5-2024

Development and Testing of an 8-Bit Digitally Throttled Hybrid Rocket Motor

Trevor W. Coombs
Utah State University, trevor.coombs@usu.edu

DEVELOPMENT AND TESTING OF AN 8-BIT DIGITALLY THROTTLED HYBRID ROCKET MOTOR

by

Trevor W. Coombs

A thesis submitted in partial fulfillment
of the requirements for the degree

of

MASTER OF SCIENCE

in

Aerospace Engineering

Approved:

Stephen A. Whitmore, Ph.D. Major Professor	Som Dutta, Ph.D. Committee Member
Matthew W. Harris, Ph.D. Committee Member	Donald Cripps, Ph.D. Committee Member

D. Richard Cutler, Ph.D.
Vice Provost for Graduate Studies

UTAH STATE UNIVERSITY
Logan, Utah

2024

ABSTRACT

Development and Testing of an 8-Bit Digitally Throttled Hybrid Rocket Motor

by

Trevor W. Coombs, Master of Science

Utah State University, 2024

Major Professor: Stephen A. Whitmore, Ph.D.
Department: Mechanical and Aerospace Engineering

Hybrid rocket motors that use nontoxic nonexplosive liquid or gaseous oxidizers and inert solid fuel grains as propellants possess inherent safety characteristics. The well-known storage, transportation, and launch safety of hybrid rocket motors have the potential to dramatically reduce their operational costs compared to traditional solid- and liquid-propelled rocket motors. Another major benefit of hybrid rocket motors is their ability to perform in flight cut-off and re-ignition and throttle by controlling the pressure from the oxidizer tank into the injector. These key advantages drive hybrid rocket motors to be considered for multiple spaceflight applications. The following thesis details the design, development, and hot fire test campaign of a digital throttling valve that utilizes a cascade of individually operated control valves set in parallel. Since the 8-bit system divides the achievable total mass flow across the 8 valves, the achievable total mass flow of any single valve remains relatively low. For this reason, solenoid operated valves can be used, allowing for fast-acting and precise control. The digital throttling valve, developed by Utah State University's Propulsion Research Lab using off the shelf components, was tested with a previously well characterized 98mm hybrid rocket motor that burns gaseous oxygen and ABS plastic as propellants. The testing campaign demonstrates multiple throttle profiles, including deep throttle ramp, multi-step boxcar, and a sine wave at a frequency of 0.5 Hz. The results

of the hot fire throttle tests are presented and compared against expected results from the analytical model. The resulting data shows that the 8-bit digital throttling valve is an effective alternative to traditional position control valves and has to potential to eliminate the obstacles keeping hybrid rockets from being used in a variety of spaceflight applications.

(78 pages)

PUBLIC ABSTRACT

Development and Testing of an 8-Bit Digitally Throttled Hybrid Rocket Motor

Trevor W. Coombs

Hybrid rocket motors that use a solid fuel grain and liquid oxidizer are low-cost and safer alternatives to traditional rocket motors. Another benefit of hybrid rocket motors is that during a burn, the amount of oxidizer into the combustion chamber can be changed, this capability is called throttling. To take advantage of the throttling ability of hybrid rocket motors, a throttling valve made up of 8 individually controlled valves is designed, developed, and tested, which is documented in this thesis. The results of the testing campaign show that the 8-bit digital throttling valve technology is an effective throttling technology and can help hybrid rocket motors become a more widely used propulsion alternative in a wide range of spaceflight applications.

ACKNOWLEDGMENTS

First, I am grateful to God for His guiding hand as I worked on this thesis and the knowledge He gave me.

I want to thank my advisor Dr. Stephen A. Whitmore for his mentorship and advice he offered throughout my Graduate education. He gave me the chance to work in the Propulsion Research Lab at USU, be a part of some incredibly fascinating projects, and helped shape my career.

I thank my family and friends for their encouragement and belief in me. I am thankful to the other student researchers in the PRL who helped me accomplish this research.

Lastly, I am grateful to my wife Madison for always supporting me and being there by my side to cheer me up when I became discouraged. I would not have been able to do this without her.

Trevor W. Coombs

CONTENTS

LIST OF TABLES

LIST OF FIGURES

NOMENCLATURE

Roman Symbols

O	oxidizer propellant
F	fuel propellant
C	carbon
H	hydrogen
N	nitrogen
T_0	combustor or stagnation flame temperature, $^\circ C$
M_w	molecular weight, $kg/kg - mol$
c^*	characteristic velocity, m/s
P_r	Prandtl number
$\dot{m}$	mass flow rate, kg/s
C_d	discharge coefficient
A	cross-sectional area, m^2
P	pressure, kPa
G	mass flux, $kg/m^2 - s$
$\dot{r}$	fuel regression rate, m/s
a	burn coefficient
n	bun exponent
m	burn exponent length
L	fuel grain length, m
$\dot{P}_0$	chamber pressure rate, kPa/s
A_{burn}	fuel port surface burn area, m^2
v	volume, m^3
R_g	specific gas constant, $J/kg - K$
A^*	nozzle throat area, m^2

Roman Symbols

K_n	choked flow parameter
V	voltage, V
Q	volumetric flow rate, $SCFH$
SG	specific gravity
t	burn duration, s
M	mass, kg
r	fuel port radius, m
A^*	nozzle throat area, m^2
c	velocity, m/s
f	thrust, N
i	frequency index
k	time index

Greek Symbols

γ	ratio of specific heats
ρ	density, kg/m^3
Δ	consumed

Subscripts

ox	oxidizer
inj	injector
c	combustion chamber
0	stagnation
L	longitudinal mean
in	inlet
∞	freestream
tot	total
e	exit

ACRONYMS

USU	Utah State University
PRL	Propulsion Research Laboratory
ABS	Acrylonitrile Butadiene Styrene
GOX	Gaseous Oxygen
O/F	Oxidizer-to-Fuel
NASA	National Aeronautics and Space Administration
CEA	Chemical Equilibrium with Applications
TGLAS	Towed-Glider Launch Assist System
DAQ	Data Acquisition
VI	Virtual Instrument
P&ID	Piping & Instrumentation Diagram

CHAPTER 1
INTRODUCTION

1.1 Motivation

Hybrid rocket motors that use nontoxic, nonexplosive liquid or gaseous oxidizers and inert solid fuel grains as propellants possess safety characteristics that have been well-known for decades [1]. The storage, transportation, and launch safety of hybrid rocket motors have the potential to dramatically reduce their operational costs compared to traditional solid- and liquid-propelled systems. When compared to similarly sized solid-propelled systems, hybrid-propelled systems have a higher dry-mass fraction. However, hybrids have performance capabilities that cannot be matched by solid-propelled rockets. Hybrid rocket motors have demonstrated their ability to perform on-demand ignition, in flight cut-off, and re-ignition [2–5], and can be deeply throttled while maintaining stable combustion [6,7]. Several studies, including as those by Casalino and Pastrone (2013) [8], (2015) [9], (2016) [10], (2019) [11], and Betts [12] have shown that when these performance capabilities are properly optimized, hybrid rocket motors can outperform solid- and mono-propellant systems, and may match the performance of more complex and expensive bi-propellant while exploiting the use of closed-loop thrust control.

These key advantages drive hybrid rocket motors to be considered for multiple spaceflight applications. These applications include sounding rockets [13, 14], orbital insertion for SmallSats and CubeSats [15], upper stages for Nano-launchers, and ascent vehicle for Lunar and Mars sample return missions [16]. A restartable and deep-throttleable hybrid rocket motor could provide a less complex and safer alternative to liquid engines and a more efficient alternative to cold gas or mono-propellant thrusters for station keeping and on-orbit maneuvering functions. This thesis outlines the design, development, and testing

of a digital throttling valve system that aims to enhance the effectiveness of a hybrid rocket motor in these possible applications.

1.2 Background

Hybrid rocket motors exhibit distinct combustion characteristics that unfortunately makes achieving precise closed-loop control difficult to do in practice. Unlike solid rocket motors where the combustion properties, including rate of fuel regression and associated oxidizer-to-fuel (O/F) ratio, can be fine-tuned and controlled during the propellant mixing and casting process and liquid rocket motors where the mixture ratio can be controlled directly through throttling; the O/F ratio and fuel regression rate vary continually throughout the burn of a hybrid rocket motor [17]. Fig. 1.1 shows the complicated and often unpredictable fluid mechanical and heat transfer phenomena within the flame zone and boundary layer that govern the rate of fuel pyrolysis during the hybrid rocket motor combustion process.

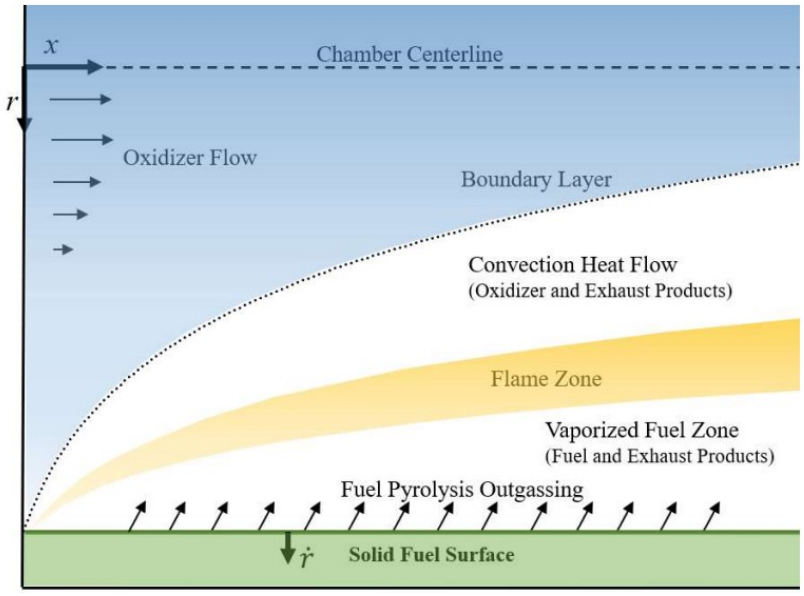

Fig. 1.1: Hybrid rocket motor combustion process.

Thus, hybrid rocket motors show a greater degree of variation in burn-to-burn characteristics, including specific impulse, total deliverable impulse, and mean thrust level. Slight variations in burn-to-burn characteristics for an experimental propulsion system is acceptable, but for hybrid rocket motors to be considered for commercial spaceflight applications burn-to-burn inconsistencies need to be reduced. A hybrid rocket motor that is capable of accurate and deep throttle control with a fast response time is one of the most effective means of reducing burn-to-burn variability. A deep-throttled system being defined as a system capable of a thrust "turndown" ratio of 4:1 from nominal thrust levels.

1.2.1 Hybrid Rocket Motor Throttling and Development

In most configurations, hybrid rocket motors have lower performance level when compared to bi-propellant liquid rocket motors. However, the ease of throttling in hybrid rocket motors when compared to pure-liquid rockets is one advantage that could outweigh their lower performance metrics [18]. Throttling a bi-propellant liquid rocket motor requires using the upstream feed pressure and injector flow area to directly control the oxidizer and fuel mass flow rates. To achieve stable combustion, a sufficiently high pressure drop across the injectors needs to be maintained or else the proper atomization levels of the propellant will not be satisfied [19]. Therefore, in liquid rockets there exists a minimum required pressure drop across the injector, known as the injector pressure ratio (IPR), of 1.25 or greater. Throttling a bi-propellant liquid rocket motor by reducing the propellant flow rates causes the injector pressure to drop faster than the chamber pressure. If the pressure ratio in a liquid rocket motor drops below the limit, coupling occurs between the chamber and propellant feed system, which precludes the engine's ability to deeply throttle. Thus, throttling bi-propellant liquid rocket motors by using feed pressure is limited to about 60-70% of nominal thrust level.

Whereas throttling a hybrid rocket motor only requires controlling the oxidizer mass flow rate by adjusting the feed pressure from the oxidizer tank into the injector. Changing the oxidizer mass flow rate indirectly affects the fuel mass flow rate, which is related to the rate of fuel pyrolysis. The fuel pyrolysis rate, also called fuel regression rate, is primarily

driven by the oxidizer mass flow rate and is responsible for setting the O/F ratio when combined inside the continuously varying cylindrical fuel port. As a result of the complex hybrid rocket motor combustion process, the O/F ratio "self-adjusts" while oxidizer mass flow rate changes during throttling. This internal regulation has a positive impact because it makes hybrid rocket motors significantly less susceptible than bi-propellant liquid rocket motors to combustion instabilities during throttling.

The serious history of throttled hybrid rocket motor development dates back about 70 years, during that time most propulsion companies in the United States, including some in Europe, were experimenting with hybrid propulsion technology [20]. One of the earliest published research projects documenting the development of a throttled hybrid rocket motor was by Moore and Bermann [21]. In their work, Moore and Bermann describe their motor as an augmented mono-propellant hydrogen peroxide motor to which they added a polyethylene solid fuel grain to increase performance. The paper mentions that the motor was easily throttled with a single valve. The study does mention however, that due to inherent instability of the hydrogen peroxide, it is difficult to vary the burn rate by more than a factor of two. Thus, limiting the ability to deeply throttle the motor.

In the 1960s, there was increased attention on throttleable hybrid rocket motors as several U.S. and European companies invested in their development for applications as sounding rockets, aerial target drones, and space launch systems. In Europe, French based propulsion company ONERA developed the Lithergol Experimental System (LEX) for use in a sounding rocket that employed hypergolic propellants composed of red fuming nitric acid and an amine fuel of meta toluene diamine/nylon [22]. The LEX rocket used a pneumatic control valve and a programmable timer to throttle from a maximum thrust level of 10,000 N to a minimum thrust level of 2,000 N, thus achieving a 5:1 turndown ratio.

During that same time two Air Force funded projects focused on the development of throttled hybrid rocket motors. The first of these developments by United Technology Center and Beech Aircraft, Franklin et al [23] and Jones [24], was Sandpiper, and aerial targeting drone, which used a combination of nitric oxide/nitrogen peroxide oxidizer and

polymethyl-methacrylate (PMMA)/magnesium fuel for propellants. The Sandpiper system had two parallel oxidizer feed lines, one which used a control valve to provide enough oxidizer to maintain thrust and the other used a valve that could accelerate the motor to a certain cruising speed before shutting off. This throttling technology helped Sandpiper achieve a turndown ratio of 8:1 from a peak thrust of 2,300 N.

The follow-on project to Sandpiper was the High-Altitude Supersonic Target (HAST) motor [25]. Compared to Sandpiper, HAST had a larger motor, used inhibited red fuming nitric acid as the oxidizer and a polybutadiene/PMMA mixture as the fuel, and used a throttling valve composed of a torque drive motor with a ball screw that actuated a pintle valve upstream of the injector. Overall, the performance of the HAST motor improved upon the earlier design and was able to reach a peak thrust level of 5,300 N with a 10:1 throttle range control.

Throughout the 1970s and 1980s the development of throttled hybrid rocket motors diminished due to the success of advancements in liquid- and solid-propelled rocket motors. The creation of the Joint Government/Industry Research and Development (JIRAD) program by NASA in the mid-1990s sparked the evaluation of two hybrid rocket boosters for a space launch vehicle [26, 27]. The first hybrid rocket motor tested was an 11-inch diameter motor designed for 13,300 N thrust and the second was a 24-inch diameter motor designed for 178,000 N thrust. Both hybrid motors had binary-operation through dual oxidizer feed lines and accomplished stepped throttling by shutting one of these oxidizer valves off. The pressure fed system achieved a throttle turndown ratio of 1.6:1 and the pump fed system achieved a 2.4:1 throttle turndown ratio.

In recent years, several academic research institutions have developed throttle capable hybrid rocket motors. The University of Arkansas at Little Rock (UALR) developed an experimental hybrid rocket motor that could throttle the oxidizer mass flow rate between 18 and 37 g/s using an oxidizer delivery system that utilized a Teledyne-Hastings HFC307 control valve [28]. Student researchers at Purdue University have demonstrated the ability to command a square wave throttle profile modeling that of a boost/sustain/boost phase

for use in tactical missile applications [29]. A throttling range turndown ratio of 10:1 was accomplished with the use of a ball-type position control valve.

Throttled hybrid rocketry development began at Utah State University's (USU) Propulsion Research Laboratory (PRL) in 2010 utilizing an electronic proportional valve to throttle a 10 N motor burning gaseous oxygen (GOX) and acrylonitrile butadiene styrene (ABS) as propellants. In 2011, an 800 N motor burning nitrous oxide and hydroxyl terminated polybutadiene as propellants was developed [6, 30]. The system employed a ball-type mass control valve controlled by an electro-mechanical actuator to throttle the motor through a 67:1 turndown ratio. Later, the PRL modified the previously discussed hybrid rocket motor to burn GOX and ABS propellants designed as a launch assist motor for NASA's Towed-Glider Launch (TGLAS) Platform [31]. This system used an upgraded throttle control valve that allowed for faster response times compared to the motor in Refs. [6] and [30]. The system achieved a throttle turndown ratio of 5:1. Both developments applied proportional, integral, derivative controller to track various prescribed throttle profiles.

1.2.2 Response Fidelity/Time Issues Associated with Traditional Position Control Valves

In the literature review above, each of the throttled hybrid rocket motor systems developed at USU used a type of position control valve (e.g., proportional valve, ball valve) to restrict the flow of oxidizer to achieve throttle control. Traditional position control valves have their benefits, but also have operational limitations. Electronic proportional valves show good response fidelity but have limited mass flow rates (< 10 g/s) and low-pressure capability (25-40 psig). Ball-type position control valves allow for high mass flow rates but require a sizable torque input to adjust the position of the valve, which causes slow flow control response times. Ball-type position control valves also have a highly non-linear flow coefficient (C_v) actuation response. The flow coefficient as a function of actuation position for several ball-valve configurations is plotted in Fig. 1.2

Note how there exists a narrow range over which each of the ball-valve configurations are effective. When the circular ball-valve, represented by a darker blue plot, is first opened, the

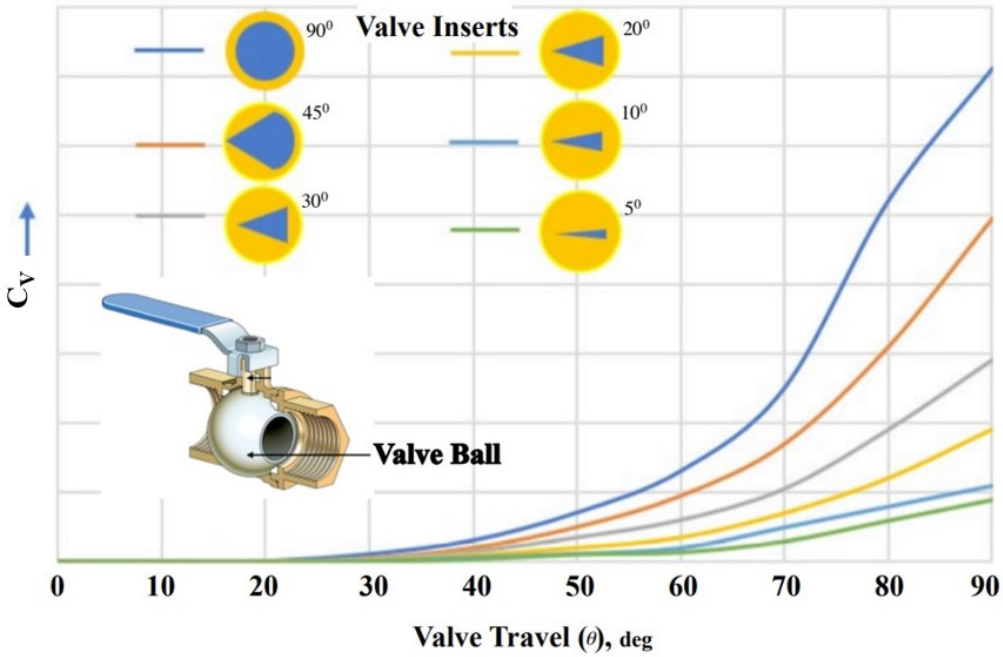

Fig. 1.2: Ball-valve flow coefficient as a function of valve travel angle.

port requires substantial position changes to reflect even minor changes in the flow control. This same response is also measured for the v-port ball valve of varied sizes. Counter to this response, when the circular ball-valve's position is nearly fully open, minor changes to actuation position result in substantial changes to the flow. These results show that circular ball-valves have poor response fidelity. As the v-port ball-valves reduce to smaller angles, the response becomes more linear. However, this leads to a substantial restriction on mass flow rate because the highest achievable flow coefficient is exceptionally low.

Fig. 1.3 illustrates the throttling response of the TGLAS system. The plot shows the closed-loop behavior of a circular ball-valve to a prescribed boxcar step thrust profile. Note the lag in response time when the first step down command is delivered, and how the thrust level exceeds its target commanded thrust on the step up. The responses can be attributed to the circular ball throttle valve's actuation latency and non-linear C_v response.

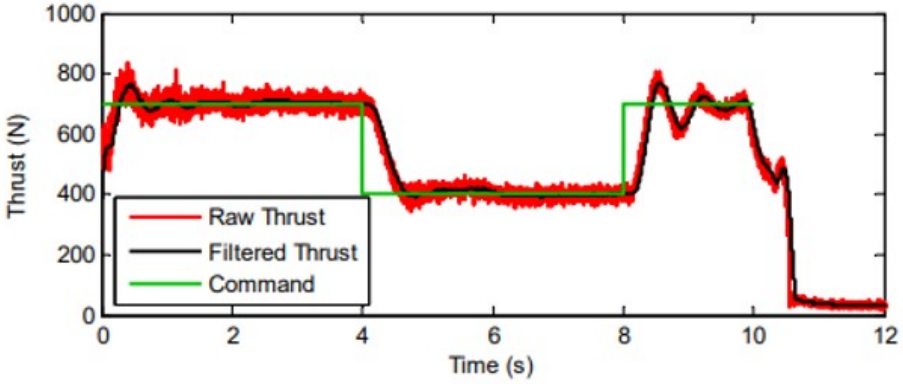

Fig. 1.3: Throttle response for the TGLAS hybrid rocket motor.

1.2.3 The Digital Valve as a Throttling Alternative to Traditional Position Control Valves

Over the past year, the PRL has been working on maturing a digital throttling valve technology with the support from the Marshall Space Flight Center's (MSFC) Valves, Actuators, Lines and Ducts Design and Development Branch. A prototype configuration consisting of 6 on/off control valves was developed by MSFC and tested at the PRL [32]. The PRL is presently working on a digital throttling valve concept that builds on that previous work.

Fig. 1.4 shows the high-level schematic for the 8-bit (binary digit) digital throttling valve concept. In the proposed concept, 8 binary solenoid operated valves (SOVs) are placed in parallel between an inlet and an outlet flow manifold. Each SOV is connected to a flow restriction orifice that has a C_v roughly half that of the next largest valve. With 8 SOVs in parallel, any of 256 possible combinations of C_v set points can be commanded. The total mass flow is divided among the 8 electrically powered solenoid valves, so high mass flow rates are attainable. Compared to a traditional position control valve, the response time of the digital valve will be 5 times faster because of the electronic actuation of the solenoid valves. As described in section 1.2.1, hybrid rocket motors only require control of the oxidizer flow to command the throttle. Since this digital throttling valve concept has

the ability to regulate one flow path, hybrid rocket motors provide an excellent application to test the effectiveness of this technology.

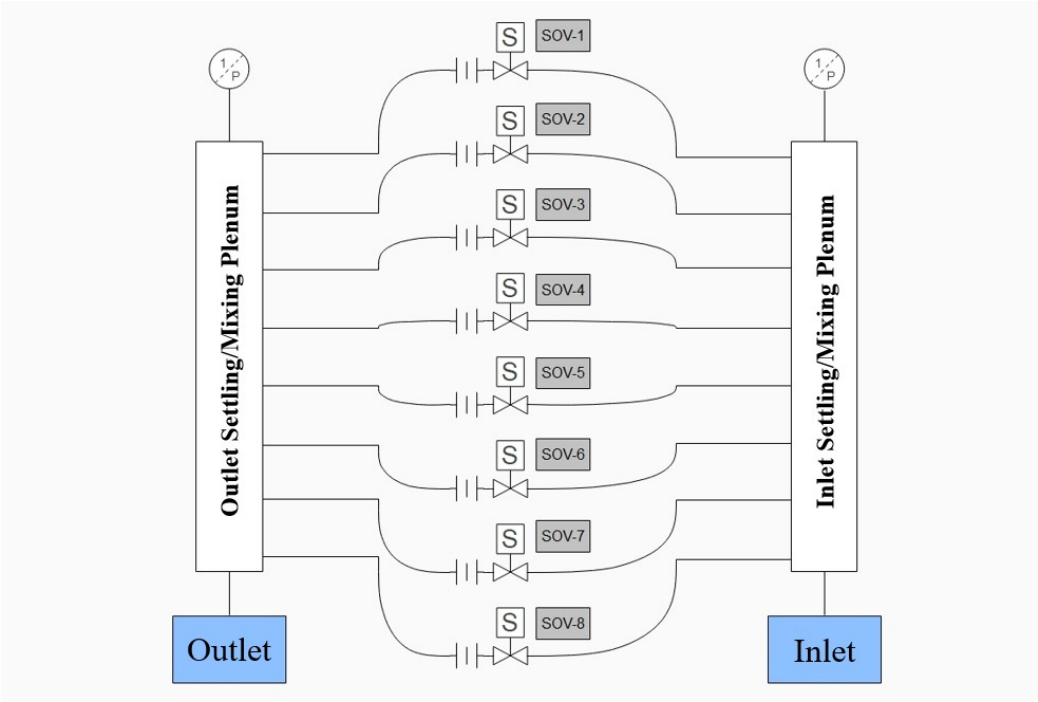

Fig. 1.4: 8-bit digital valve schematic.

1.2.4 Analytical Modeling of Hybrid Rocket Combustion

To determine the effectiveness of the digital throttling valve from the data collected during the test campaign, a 1-dimensional ballistic analytical model of the hybrid rocket motor's combustion dynamics is developed. This allows for the effects of the mechanical response of the oxidizer throttling valve and the effects due to fuel pyrolysis on the response fidelity to be characterized separately.

(a) *Combustion Chamber Pressure*

The longitudinal mean combustion chamber pressure rate is given in Eq. (1.1). This equation was developed by Eilers and Whitmore (2008) [33], and modified for

compressible flow by Whitmore (2019) [34], by applying the compressible-flow conservation equations across the hybrid fuel combustion port

$$\dot{P}_{0_c} = \frac{A_{burn}\dot{r}_L}{V_c} \cdot [\rho_{fuel} R_{g_c} T_{0_c} - P_{0_c}] - P_{0_c} \cdot \left[\frac{A^*}{v_c} \sqrt{\gamma_c R_{g_c} T_{0_c} \left(\frac{2}{\gamma_c + 1} \right)^{\frac{\gamma_c+1}{\gamma_c-1}}} \right] + \frac{R_{g_c} T_{0_c}}{v_c} \cdot \left[(K_n C_d A_{inj}) \cdot \frac{P_{0_{inj}}}{\sqrt{R_{g_{ox}} T_{0_{inj}}}} \right] \quad (1.1)$$

It is useful to split Eq. (1.1) up into three distinct terms. The first term on the right-hand side is associated with the fuel regression rate and subsequent growth in combustion chamber volume. The second term on the right-hand side relates to the nozzle throat choke point. The third term on the right-hand side is a result of the flow across the oxidizer injector. The parameter K_n is dependent on whether the oxidizer flow across the injector is choked flow or not. Eq. (1.2) is for unchoked injector flow,

$$K_n = \sqrt{\left(\frac{2\gamma_{ox}}{\gamma_{ox} - 1} \right) \cdot \left(\frac{P_{0_c}}{P_{0_{inj}}} \right)^{\frac{2}{\gamma_{ox}}} \cdot \left(1 - \left(\frac{P_{0_c}}{P_{0_{inj}}} \right)^{\frac{\gamma_{ox}-1}{\gamma_{ox}}} \right)} \quad (1.2)$$

and Eq. (1.3) is for choked injector flow.

$$K_n = \sqrt{\gamma_{ox} \cdot \left(\frac{2}{\gamma_{ox}} \right)^{\frac{\gamma_c+1}{\gamma_c-1}}} \quad (1.3)$$

Choked flow means that the downstream pressure no longer has any influence on the mass flow of the flowing fluid as it passes through a constriction (such as a valve in a pipe), only the upstream pressure. Choked flow occurs when the ratio of the absolute upstream pressure to the absolute downstream pressure is equal to or greater than the minimum pressure ratio, shown in Eq. (1.4)

$$\frac{P_{in}}{P_{out}} \geq \left(\frac{\gamma + 1}{2} \right)^{\frac{\gamma}{\gamma-1}} \quad (1.4)$$

For oxygen, the minimum pressure ratio is about 1.893, since $\gamma_{ox} \approx 1.4$. The oxidizer mass flow rate is calculated in Eq. (1.5).

$$\dot{m}_{ox} = (K_n C_d A_{inj}) \cdot \frac{P_{0_{inj}}}{\sqrt{R_{g_{ox}} T_{0_{inj}}}} \tag{1.5}$$

With combustion chamber pressure calculated, thrust, mass flow, and other performance related parameters are calculated using the standard 1-dimensional de Laval flow equations [35].

(b) *GOX/ABS Combustion Chemistry*

Calculating the chemical composition of the combustion plume products and the resulting thermodynamic and transport properties is a complicated process. Fortunately, scientists at the NASA Glenn Research Center have developed a computer program called Chemical Equilibrium with Applications (CEA) to solve such calculations. The agency describes CEA on their website as, "A program which calculates chemical equilibrium product concentrations from any set of reactants and determines thermodynamic and transport properties for the product mixture" [36].

To determine the thermodynamic and transport properties for the product mixture, CEA needs specific reactant properties including, the enthalpy of formation of the fuel to account for the decomposition energy of the reaction and the chemical formula of ABS. Whitmore [37] describes how the enthalpy of formation of ABS fuel, 62.63 kJ/mol, was previously derived using the "group addition" method. Whitmore et al. [38] also previously performed Fourier Transform Infrared (FTIR) spectroscopy tests to approximate the monomer ratio of acrylonitrile (C_3H_3N), butadiene (C_4H_6), and styrene (C_8H_8) in ABS to derive the chemical formula of extruded ABS in Eq. (1.6).

$$ABS = C_{3.85}H_{4.85}N_{0.43} \tag{1.6}$$

CEA calculates the thermodynamic and transport properties of ABS/GOX combustion as a function of the combustion chamber pressure and the O/F ratio. The

CEA-calculated parameters are 1) T_{0_c}, combustion flame temperature, 2) M_w, molecular weight, 3) γ_c, ratio of specific heats of the combustion chamber combustion products, 4) c^*, characteristic velocity, 5) P_r, Prandtl number, 6) μ, dynamics viscosity. 2-dimensional linear interpolation property tables with O/F ratio and chamber pressure as independent lookup values, Fig. 1.5, are generated from the resulting CEA calculations.

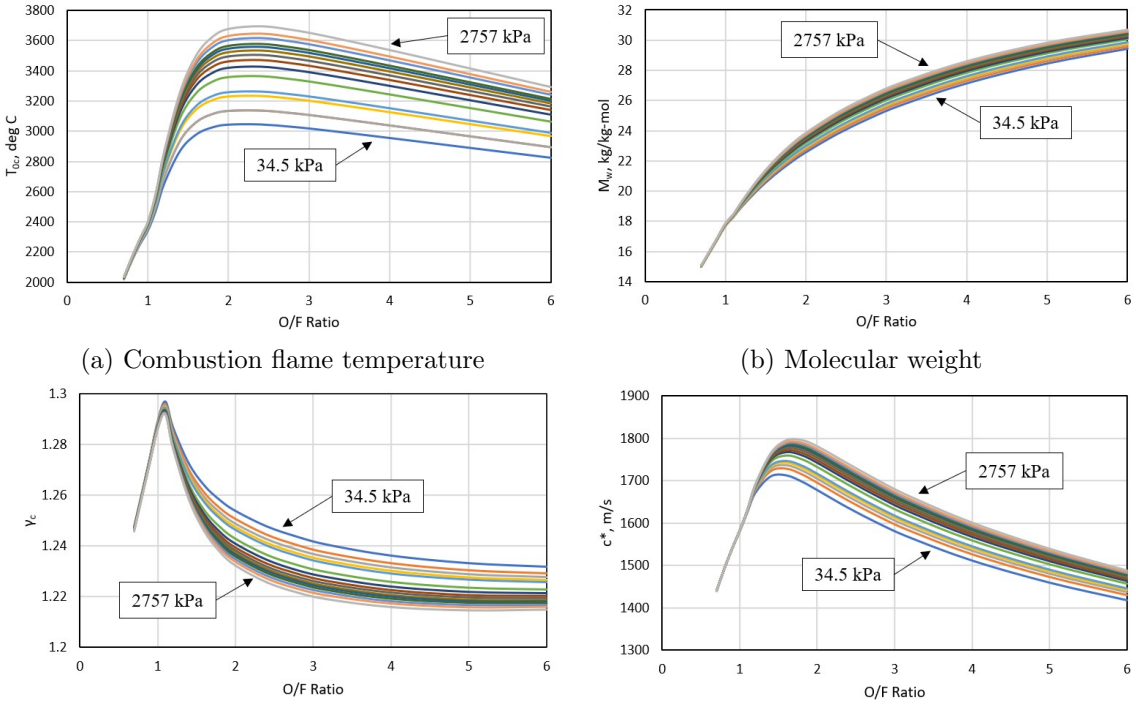

(a) Combustion flame temperature

(b) Molecular weight

(c) Ratio of specific heats

(d) Characteristic velocity

Fig. 1.5: CEA-derived thermodynamic property lookup tables.

(c) *Fuel Regression Rate, O/F Ratio*

During early development of hybrid rockets, Marxman and Gilbert [39, 40] demonstrated that the fuel regression rate is driven primarily by viscous heat transfer within the boundary layer. Thus, fuel regression rate has a strong dependence on the mass flux across the combustion chamber. They established a length dependent,

power-law regression rate model, called Marxman Law, represented in Eq. (1.7).

$$\dot{r}_L = a \cdot G_{ox}^n \cdot L^m \tag{1.7}$$

Where a, n, and m are empirically determined constants. Initial studies predicted a value for m of about 0.2 for the parameter in Eq. (1.7). Initial Fuel mass flow rate is calculated as a function of the fuel regression rate in Eq. (1.8).

$$\dot{m}_{fuel} = \rho_{fuel} A_{burn} \dot{r}_L \tag{1.8}$$

Although numerous regression rate calibrations have shown that the power-law model form for fuel regression rate in Eq. (1.7) is accurate for non-erosive burning propellants, there does not exist an exhaustive model that reliably predicts this quantity for a variety of different propellant and motor dimensions. The O/F ratio is calculated as a ratio of the oxidizer mass flow rate to the fuel mass flow rate, shown in Eq. (1.9).

$$O/F = \frac{\dot{m}_{ox}}{\dot{m}_{fuel}} \tag{1.9}$$

From Eq. (1.7), if burn exponent, $n > \frac{1}{2}$, the O/F responds with a positive shift and the motor burns *leaner*, or oxidizer rich over time. If the burn exponent is equal to $\frac{1}{2}$, then the motor experiences *no shift in O/F ratio* during a burn. Lastly, if the burn exponent, $n < \frac{1}{2}$, then the motor experiences and negative O/F shift and burns increasingly *fuel rich* over time. The O/F shift that hybrid rocket motors experience during a burn can have a dramatic effect on the observed thrust profiles. For a steady-state oxidizer flow rate, a positive O/F ratio shift will typically cause a drop off in thrust with burn time. Whereas a negative O/F ratio shift will typically cause a rise in thrust with burn time.

(d) *Thrust*

The thrust for the hybrid rocket motor is calculated using the classic rocket equations. Knowing the pressure and temperature in the combustion chamber, the free stream pressure, the ratio of specific heats of the exhaust, the specific gas constant, the cross-sectional area of the nozzle throat and exit, and the total mass flow rate the following method can be followed to determine the thrust. First the exit Mach number, $Mach_e$ is found using an iterative numerical method to solve Eq. (1.10)

$$\frac{A_e}{A^*} = \left(\frac{\gamma+1}{2}\right)^{-\frac{\gamma+1}{2(\gamma-1)}} \frac{(1+\frac{\gamma-1}{2}Mach_e^2)^{\frac{\gamma+1}{2(\gamma-1)}}}{Mach_e} \tag{1.10}$$

Having solved for the exit Mach number allows for calculation of the exit temperature, in Eq. (1.11), exit pressure, in Eq. (1.12), and exit velocity, in Eq. (1.13)

$$T_e = \frac{T_0}{(1+\frac{\gamma-1}{2}Mach_e^2)} \tag{1.11}$$

$$P_e = P_{0_c}\left(1+\frac{\gamma-1}{2}Mach_e^2\right)^{-\frac{\gamma}{\gamma-1}} \tag{1.12}$$

$$c_e = Mach_e\sqrt{\gamma R_g T_e} \tag{1.13}$$

Now, the thrust is calculated using Eq. (1.14)

$$f = \dot{m}_{tot}\cdot c_e + (P_e - P_\infty)A_e \tag{1.14}$$

The analytical thrust calculations will be compared to the thrust measurements taken during the hot fire testing campaign.

1.2.5 Frequency Response Analysis

The samples of the various signals that will be measured using sensors connected to DAQ devices on the cart and the digital valve are all time-domain representations of the signals. Time-domain representations give the magnitude of the signal at the instant of time during which it was sampled. In this case, a frequency analysis performed on the pressure and thrust measurements may provide more insights about the individual signals and the digital throttling system from which they were generated rather than just the magnitudes of the individual samples. Fourier's theorem is the underlying concept behind this transformation. As described in National Instruments' product documentation for LabVIEW [41], Fourier's theorem states that any waveform in the time domain can be represented by the weighted sum of sines and cosines. The same waveform then can be represented in the frequency domain as a pair of magnitude and phase values, called spectra, at each component frequency. The representation of a signal in terms of its individual frequency components is the frequency-domain representation of the signal.

A common, yet powerful method for characterizing frequency response relationships in terms of the frequency domain is the Fourier transform. The following equation, Eq. (1.15), defines the Fourier transform

$$F(jw) = \int_{-\infty}^{\infty} f(\tau) e^{-j[w\tau]} d\tau \tag{1.15}$$

The following equation, Eq. (1.16), defines the inverse Fourier transform

$$f(t) = \left[\frac{1}{2\pi}\right] \left(\int_{-\infty}^{\infty} F(jw) e^{j[wt]} dw \right) \tag{1.16}$$

These two equations represent a Fourier transform pair, which consists of the signal representation in both the time and frequency domain. Fourier transform pairs have been evaluated for a whole suite of functions and can be looked up using a table of Fourier transforms [42]. This analysis method is known as "frequency response."

When the waveform is digitally sampled and the function $f(t)$ is stored for discrete instants in time, as is with the signals that will be measured in this paper, discrete equations are required for numerical computation [43]. The algorithm used to transform N samples of data from the time domain into N samples of data in the frequency domain is the discrete Fourier transform (DFT). The following equation, Eq. (1.17), defines the DFT

$$Y_i = \frac{1}{N} \sum_{k=0}^{N-1} y_k e^{-j\left[\frac{2\pi}{N} \cdot i \cdot k\right]} \tag{1.17}$$

Where the function Y_n is the discrete frequency components of the waveform. The DFT of a physical signal results in a symmetric spectrum series about a frequency called the Nyquist frequency. The Nyquist frequency is the highest frequency component that should exist in the input series to yield useful results. If there are no frequencies above the Nyquist frequency the original signal can be reconstructed exactly from the samples. Any frequencies sampled above the Nyquist frequency exhibit harmonic behavior that corrupt the results.

The DFT is almost never used in practice however, because implementing the DFT on N data samples requires approximately N complex operations and is a time-consuming process [41]. The fast Fourier transform (FFT) is a fast algorithm for calculating the DFT. The FFT operates by breaking an N point time-domain signal into N time-domain signals each made up of a single point. The second step in the algorithm is to calculate the N frequency spectra that correspond to the N time-domain signals. Finally, the N spectra are synthesized in a single frequency spectrum. The most common FFT algorithms require that the number of elements in a signal sample be a power of two to correctly synthesis the signal.

1.2.6 Overview

The proceeding sections of this document will outline the objectives and approach for this thesis. The objectives section outlines the success criteria that constitutes completion of the thesis. The approach section describes the plan for accomplishing the objectives.

CHAPTER 2
OBJECTIVES

2.1 Hardware Engineering

2.1.1 Build an 8-bit digital throttle valve system capable of oxidizer mass flow rates > 50 g/s and deep throttle turndown ratio ≥ 25:1 from nominal thrust levels.

2.1.2 Build an 8-bit digital throttle valve system that is compatible with current test hardware that.

2.1.3 Design and build electrical interface to communicate with control software.

2.2 Control Software Development

2.2.1 Develop software capable of controlling the digital valve's manual and automatic operation.

2.2.2 Develop software capable of commanding various throttle profiles.

2.3 Testing and Data Collection

2.3.1 Perform calibration on digital valve to validate the accuracy of the orifice C_v values and mass flow as a function of the digital valve inlet and outlet pressures.

2.3.2 Perform 3 constant throttle calibration burns on the test motor to determine fuel regression rate coefficients

2.3.3 Collect pressure, thrust, mass, and photographic data from the rocket hot fires of a deep throttle ramp thrust profile, a deep throttle multi-step boxcar thrust profile, and a 0.5 Hz sine wave thrust profile.

2.4 Analysis of Test Results

2.4.1 Analyze the test results of the deep throttle ramp, deep throttle multi-step boxcar, and 0.5 Hz sine wave

2.4.2 Compare numerical model to experimental data.

2.4.3 Determine effectiveness of digital throttle valve.

CHAPTER 3
APPROACH

3.1 Hardware Engineering

The 8-bit digital throttling valve must be capable of oxidizer mass flow rates > 50 g/s and deep throttle turndown ratio $\geq$ 25:1 from nominal thrust levels. Valve must be compatible with all current test hardware, including the PRL's 98mm GOX-ABS hybrid rocket motor, the lab's low energy 3D-printed ignition system, and other test support equipment.

3.1.1 8-Bit Digital Throttle Valve Configuration

The 8- bit digital valve will be built using components off the shelf (COTS). Utilizing COTS rather than custom manufactured components drives costs down and minimizes down time if a component fails during the testing campaign because their replacement is readily available. The digital valve will be built to meet all performance objectives. The prototype configuration of the 8-bit digital control valve is shown in Fig. 3.1. In the prototype configuration the 8 SOV's are mounted in parallel to an inlet and outlet right angle flow rectangular manifolds. This configuration allows for SOV's 7-4 to be placed slightly above SOV's 3-0, thus leading to a more compact control valve design. Pressure transducers installed on the inlet and outlet manifolds will measure the inlet and outlet pressure of the digital throttle valve.

The total collected C_v value of the 8-bit digital throttle valve needs to be able to accommodate the anticipated high mass flow rates. The initial estimation for flow restriction orifice sizes and their expected C_v value that will be attached downstream of each SOV is displayed in Table 3.1.

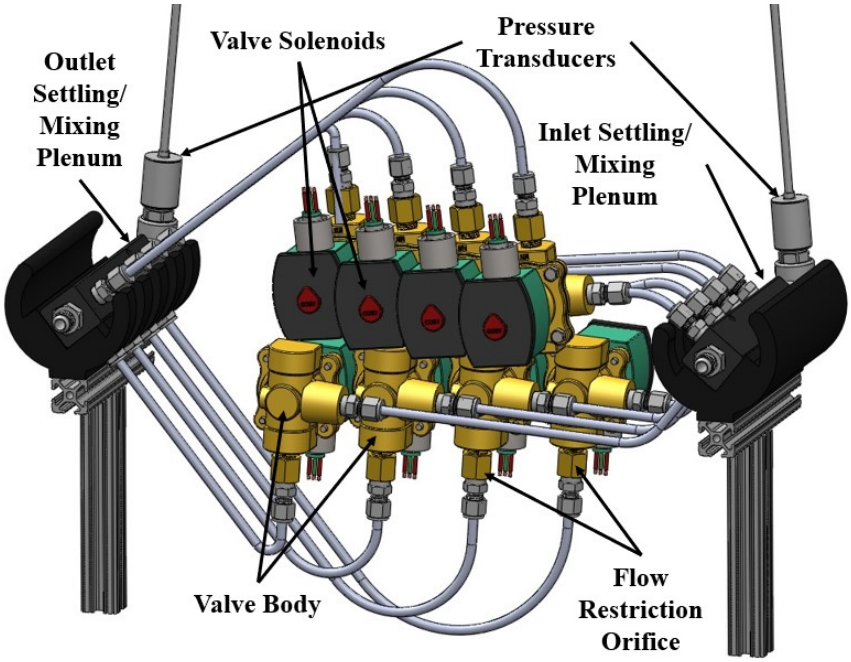

Fig. 3.1: Prototype configuration of 8-bit digital throttle valve.

Table 3.1: Initial estimation for flow restriction orifice sizes and expected C_v value.

Total Collected C_v		0.6151
SOV #	Orifice Diameter, *in*	Expected C_v Value
SOV-0	0.0102	0.0025
SOV-1	0.015	0.005
SOV-2	0.021	0.0096
SOV-3	0.029	0.019
SOV-4	0.041	0.038
SOV-5	0.060	0.081
SOV-6	0.081	0.15
SOV-7	0.113	0.31

3.1.2 98mm GOX-ABS Hybrid Rocket Motor

The article used for this testing campaign is a 98mm hybrid rocket motor that uses gaseous oxygen (GOX) as the oxidizer propellant and acrylonitrile butadiene styrene (ABS) as the solid fuel propellant. This combination of propellants has favorable performance and reliability traits which has been proven by the multiple testing campaigns conducted at the PRL [5,31,44]. This well characterized motor operates at a nominal chamber pressure of approximately 140 psia (965 kPa) and produces a nominal thrust level of 200 N. Fig. 3.2 shows

the 98mm motor cross-section along with labeled motor components and outer dimensions. Below this figure, Fig. 3.3 displays the major components of the 98mm hybrid rocket motor. Starting from the top from left to right the motor components are; Phenolic liner, extruded ABS fuel grain (burnt), Cessaroni Pro98 4-G Motor Case, threaded nozzle retaining ring, threaded injector retaining ring, graphite nozzle assembly with throat diameter of 1.397 cm and a 3.54 expansion ratio, injector cap, and FDM-printed ABS Arc-Ignition Cap.

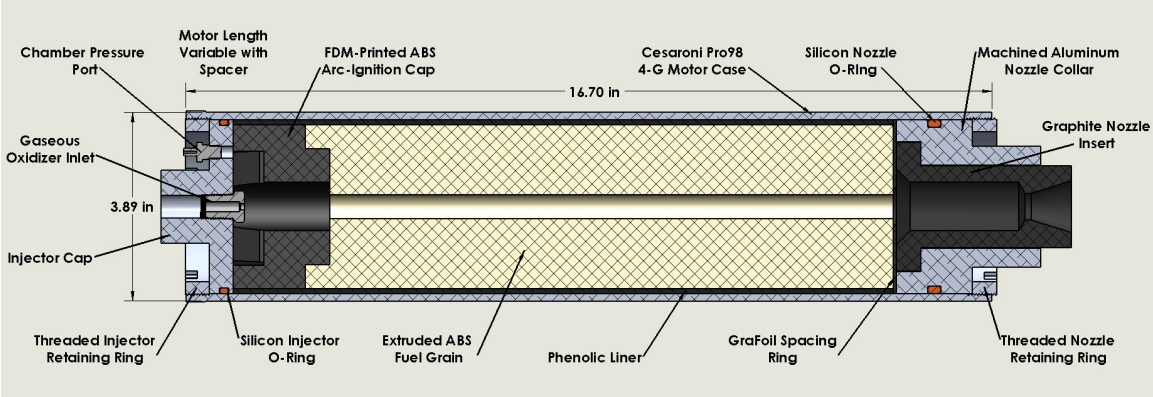

Fig. 3.2: Cross-section of 98mm hybrid rocket motor.

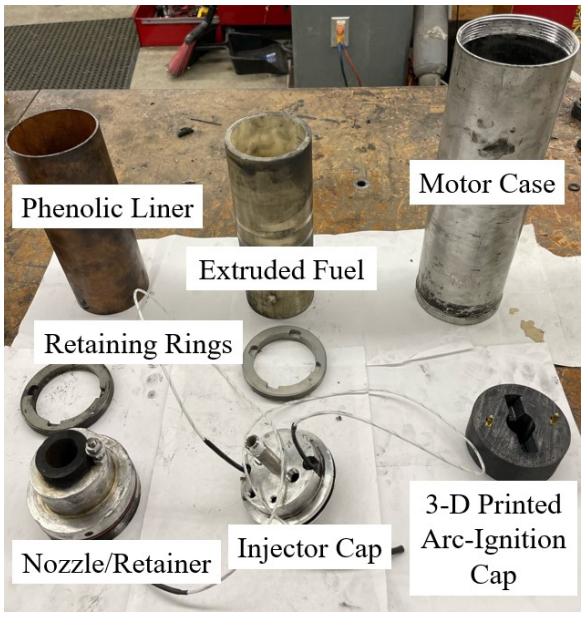

Fig. 3.3: 98mm hybrid rocket motor major components.

3.1.3 Motor Ignition System

The combustion process for the hybrid rocket motor begins with an ignition source that ignites the oxidizer flow into the combustion chamber. This ignition depends on the FDM printed ABS low-wattage, arc-ignition cap, a USU patented technology [45]. The power needed for the arc-ignition to take place relies on an UltraVolt® high-voltage power supply (HVPS) unit. Once initiated, the HVPS sends a current-limited (60 mA) high voltage signal of up to 30 Watts. The dispersed voltage is dependent upon the level of impedance through the path of the arc and varies between 100 to 250 volts. Each recurring ignition draws less than 10 Watts and uses about 3-10 joules of energy. This technology allows the motor to be restarted multiple times during the lifetime of the arc-ignition cap.

Unlike the fuel grain itself, which is machined to dimension from commercially available extruded ABS rods, the arc-ignition cap is FDM, or 3-D, printed using commercial ABS filament. The arc-ignition cap is printed at full in-fill density. Two slots are printed into the part where two electrodes are inserted that interface with the injector cap. Embedded wires run from each electrode towards the center of the arc-ignition cap and provide the path for the high-voltage current. The high-voltage current arcs between the wires and "carve" a path through the 3-D printed ABS material, as shown in Fig. 3.4.

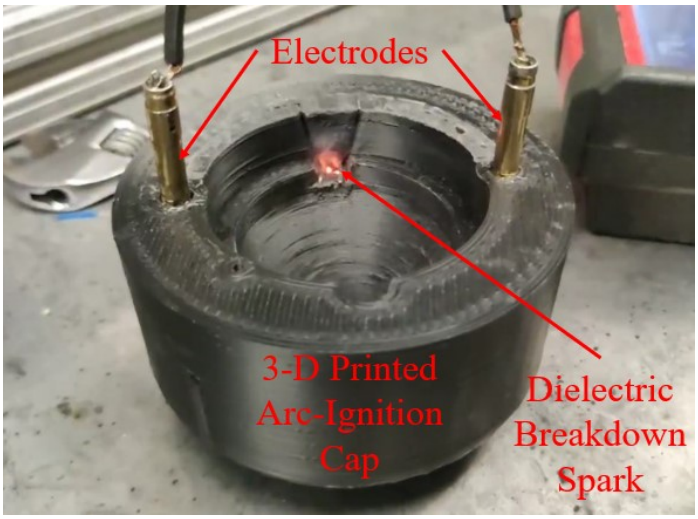

Fig. 3.4: Arc-ignition demonstration.

Printing ABS changes its electrostatic breakdown properties. which enables an inductive spark within the material to ignite the oxidizer for combustion. Since combustion begins in the arc-ignition cap it becomes part of the consumed fuel during a burn, which is the lifetime limiting factor.

3.1.4 Motor Test Support Equipment

To perform static fires for the testing campaign of the digital throttle valve, a testing apparatus, which industry professionals commonly refer to as a "test cart" is used. The test cart carries all the essential electronics, DAQ measurement hardware, sensors, oxidizer tanks, sturdy framing, and piping to run a static fire hybrid rocket test, as shown in Fig. 3.5. Rather than having a dedicated permanent test stand for static rocket fires, the test cart enables convenient transportation from the PRL's assembly area to USU's propulsion test cell, also known as the BLAST Lab. Once the test cart is secured in the BLAST Lab, all functional checks are made according to the pretest procedure list and a static fire test is ready to proceed.

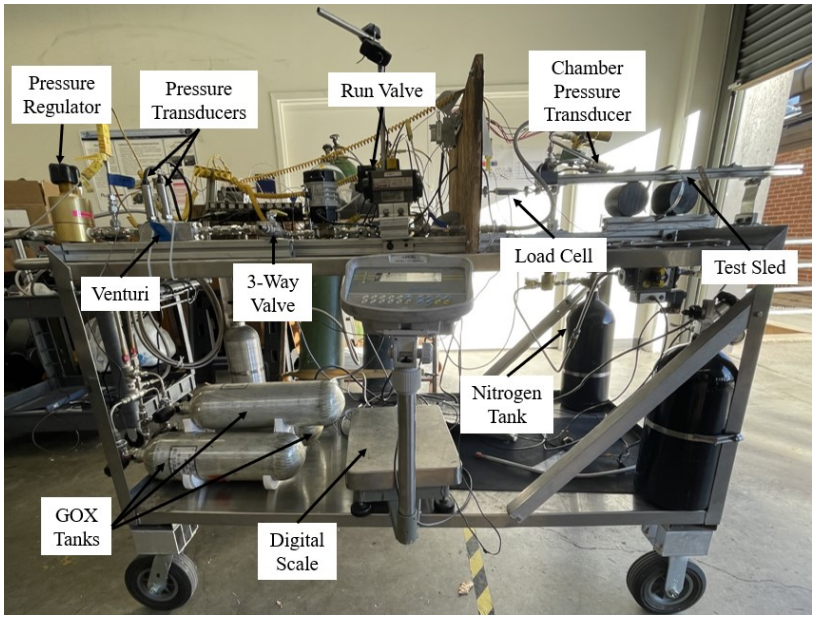

Fig. 3.5: Test cart for 98mm hybrid rocket motor equipment.

Figure 3.6 below shows the test cart's piping and instrumentation diagram in a clearer format. Pictured in diagram are first the GOX tanks that supply oxidizer to the system, which run through a pressure regulator valve. The GOX then flows into the venturi, which researcher use to measure the oxidizer's massflow rate, before entering the digital throttling valve inlet. After the oxidizer exits the digital throttling valve it passes through a run valve that is actuated by a gaseous nitrogen (N_2) supply tank. Following a hot fire, the run valve switches to the gaseous nitrogen supply and uses the inert gas to act as a purge system to flush out any unused GOX to prevent unintentional combustion. The oxidizer goes from the run valve through piping to the 98mm motor's injector cap into the gaseous oxidizer inlet where it contacts the solid fuel allowing for combustion to occur.

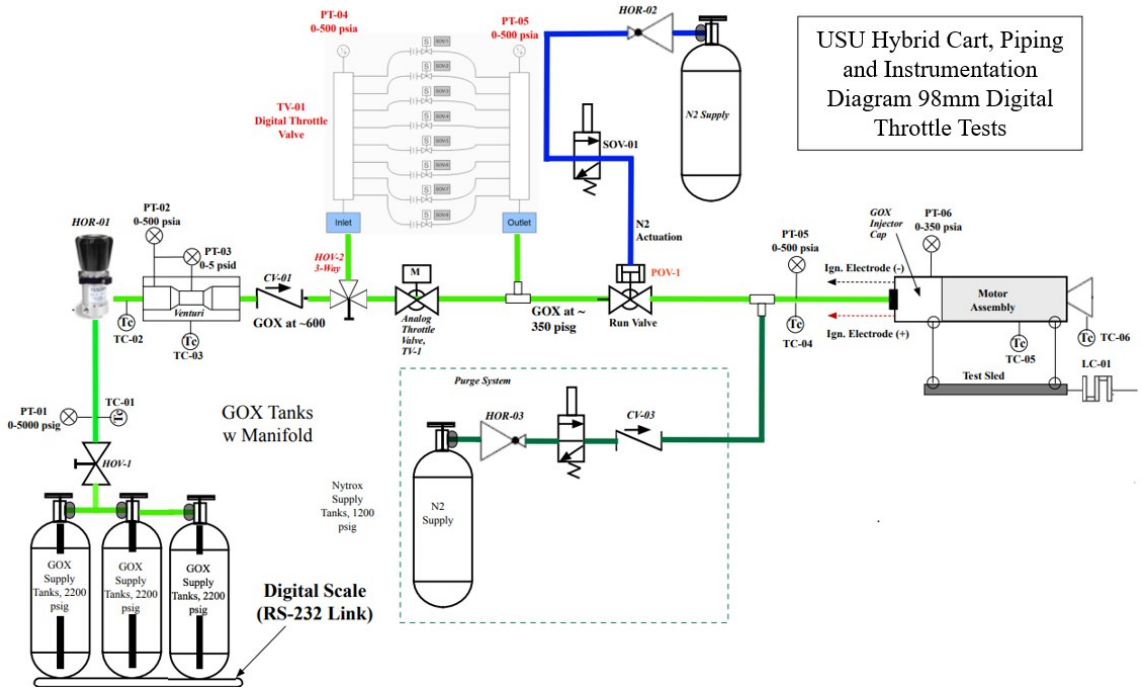

Fig. 3.6: Test support equipment piping and instrumentation diagram (P&ID).

3.1.5 Digital Valve Electrical Interface Configuration

The electrical interface for the digital valve will feature rail mounted solid-state relays that convert the SOVs from A/C input power to DC control logic, as shown by Fig. 3.7.

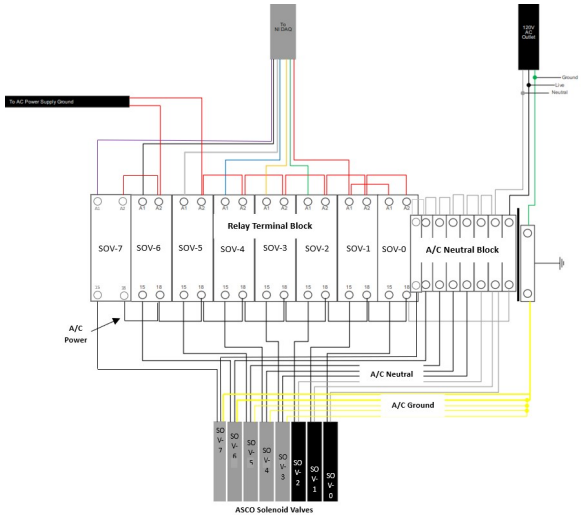

Fig. 3.7: 8-bit digital valve wiring schematic.

Each SOV's control logic will be sent using a National Instruments (NI) DAQ module, which will be connected to a laptop running the control software via Universal Series Bus (USB), as shown in Fig. 3.8. The DAQ device also measures the voltage signals produced from the pressure transducers attached at the inlet and outlet of the valve.

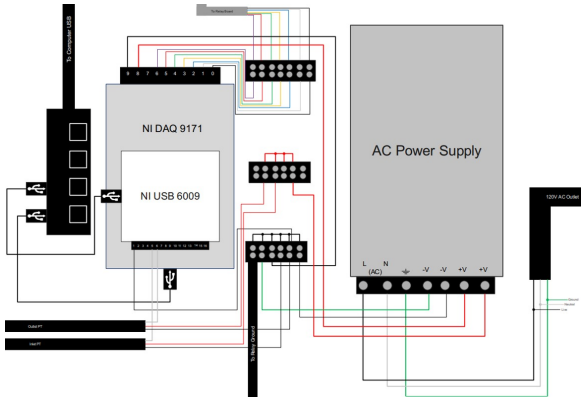

Fig. 3.8: NI DAQ wiring schematic.

3.2 Control Software Development

Existing LabVIEW software that was developed for testing the MSFC throttle valve was modified to include additional manual controls and automatic operation for the 2 added SOVs. A screenshot of the control software front panel is shown in Fig. 3.9.

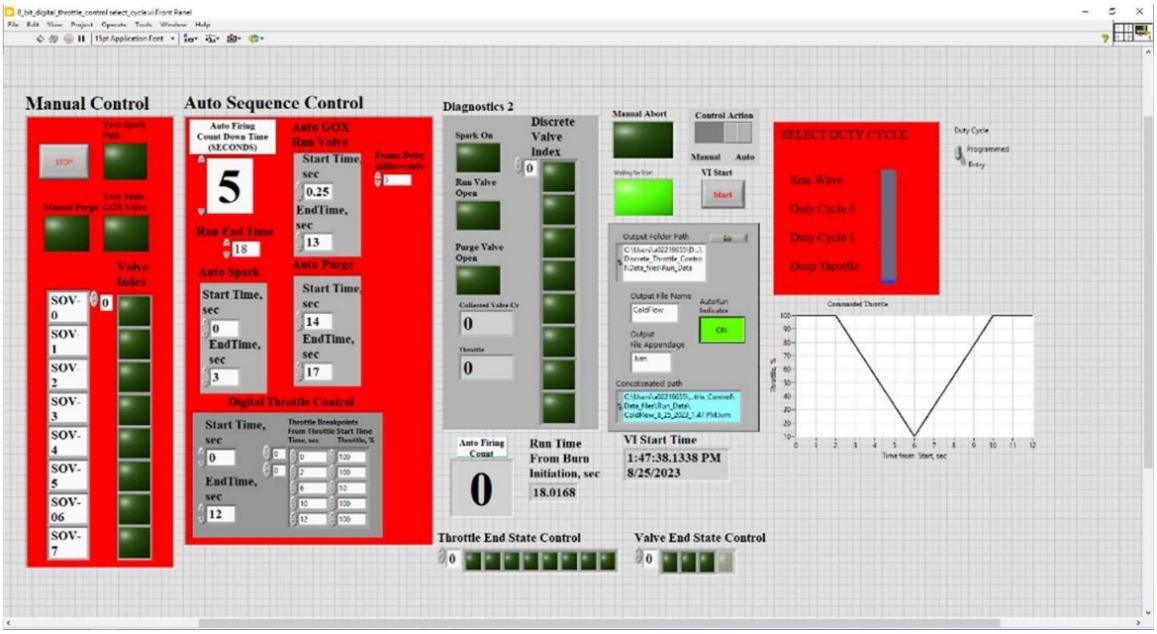

Fig. 3.9: LabVIEW control software front panel.

3.3 Testing and Data Collection

Testing of the 8-bit digital throttling valve will include calibration of various test systems and calculation parameters and a data collection phase that has been deemed as the testing campaign.

3.3.1 Digital Valve C_v and Mass Flow Calibration

The digital throttle valve calibration will validate the accuracy of the orifice C_v values and mass flow as a function of the digital valve inlet and outlet pressures in preparation for the testing campaign, the set-up is illustrated in Fig. 3.10. Compressed gaseous nitrogen (N_2) will be used as the working fluid for the cold flow tests since it is an inert gas and behaves like GOX. Each of the 8 SOV are actuated individually at inlet pressures varying from 100 psi to 500 psi in 100 psi increments. A tank scale for the N_2 will measure the pre- and post-tank mass, which will be used to calculate the mean valve N_2 mass flow for each valve. Thermocouple measurements at the inlet and outlet of the digital throttle valve will be used for volumetric flow and flow density calculations.

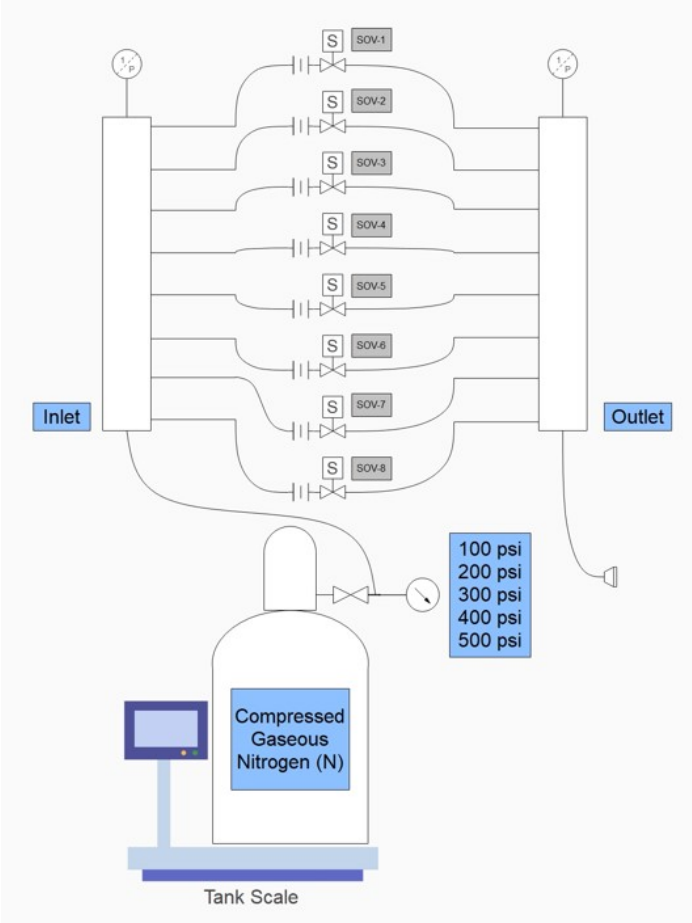

Fig. 3.10: Digital throttle valve calibration set-up.

3.3.2 Hybrid Motor Regression Rate Calibration

A set of 3 steady-state burns will be performed on a single new fuel grain to measure the variation in fuel regression rate over time. Each burn will feature 100% commanded throttle for 15 seconds. These calibration tests will help characterize the burn coefficients for the fuel regression rate calculation described in the analytical modeling section for regression rate (c).

3.3.3 Hot Fire Testing Campaign

The data collected during the testing campaign will include pressure data, measured with pressure transducers, thrust data, measure with a load cell, mass data, measured with a lab scale, and photographic data, taken with a mobile phone and an action camera equipped with a welding glass for visualization of the plume. Fig. 3.11 displays the commanded throttle duty cycles as a function of time for the hot fire testing campaign. The commanded throttle patterns are a deep throttle ramp thrust profile, Fig. 3.11a, a deep throttle multi-step boxcar thrust profile, Fig. 3.11b, and a 0.5 Hz sine wave thrust profile, Fig. 3.11c.

3.4 Analysis of Test Results

As detailed in section 1.2.4, an analytical model be adjusted to correlate with experimental data gathered during the calibration tests and hot fire testing campaign. Experimental data will be compared against expected results from the analytical model. Conclusions from this correlation will be used to quantify the effects of the digital throttling valve on the hybrid rocket motor's mass flow rate and turndown ratio. A frequency analysis will also be performed on the resulting hot fire data to assess the frequency response of the digital valve system. The analyzed data will be used to determine the effectiveness of the digital throttling valve as a higher performing alternative to traditional position control throttling valves.

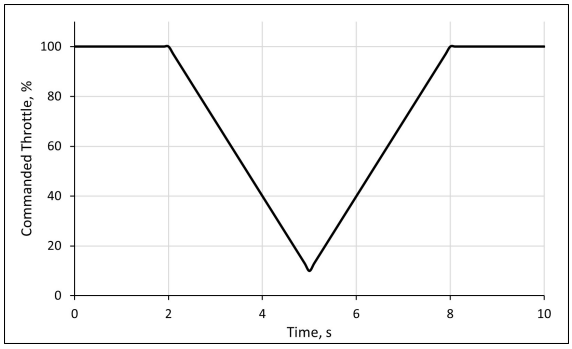

(a) Deep throttle ramp thrust profile

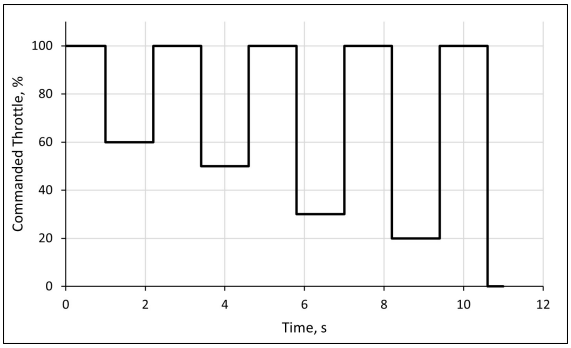

(b) Deep throttle multi-step boxcar thrust profile

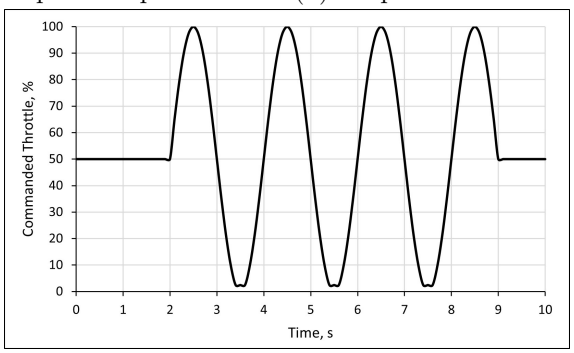

(c) 0.5 Hz sine wave thrust profile

Fig. 3.11: Commanded throttle duty cycles.

3.5 Schedule

This section outlines when each objective is anticipated to be accomplished as shown in Fig. 3.12.

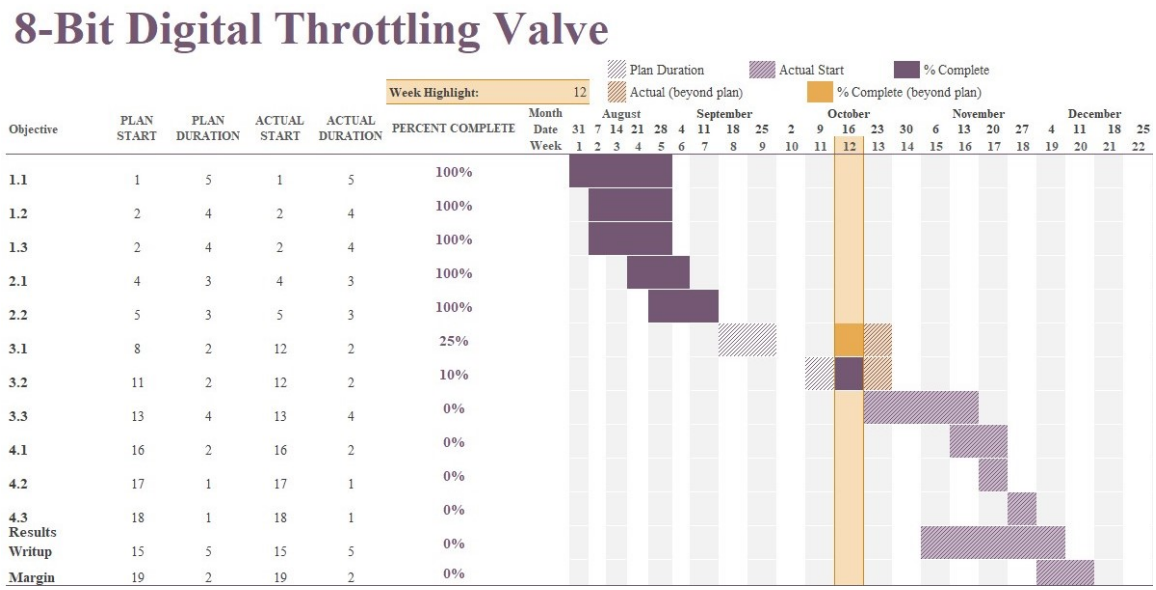

Fig. 3.12: Gantt chart schedule.

CHAPTER 4

RESULTS

This section presents results from the 8-bit digital throttle valve testing campaign. The final design of the 8-bit digital valve and its associated components is presented first. Results from the digital valve C_v and mass flow calibration test are presented next. Calibration results are followed by data from the motor regression rate calibration tests. Next, results from the deep throttle ramp test, deep throttle multi-step boxcar duty cycle test, and sine wave throttle test are presented and compared to analytical predictions. Finally, future work for the 8-bit digital throttle valve technology is identified.

4.1 8-Bit Digital Throttle Valve Configuration

The configuration of the 8-bit digital throttle valve used for testing closely resembles the prototype configuration described in section 3.1.1. Figs. 4.1, 4.2, and 4.3 show the final design at three different angles.

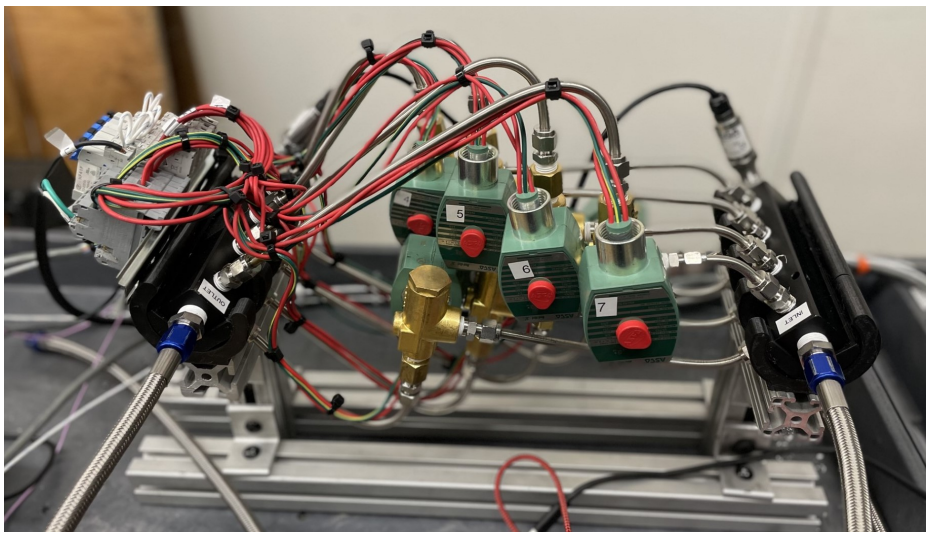

Fig. 4.1: Test configuration of 8-bit digital throttling valve.

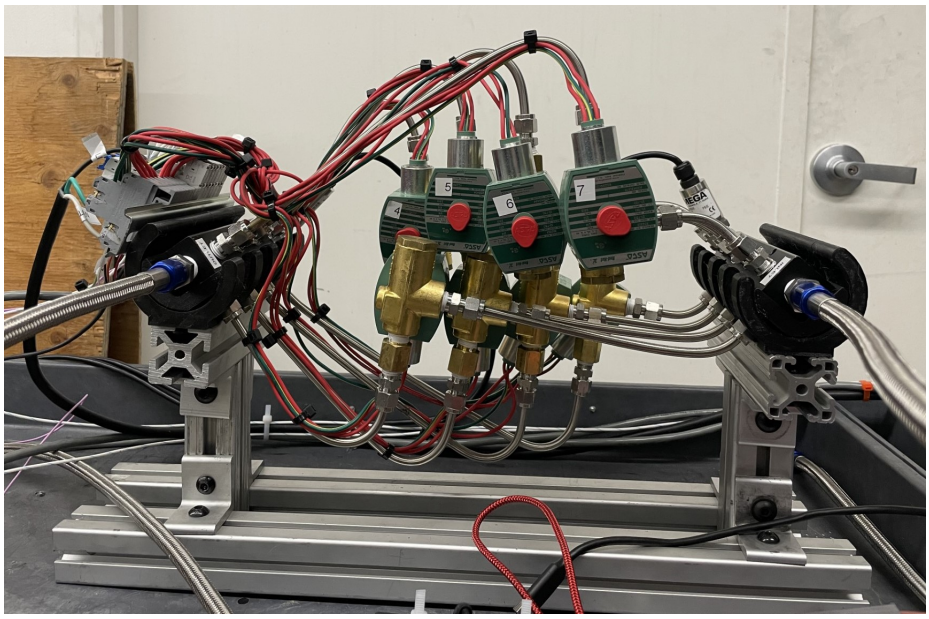

Fig. 4.2: Front view of 8-bit digital throttling valve.

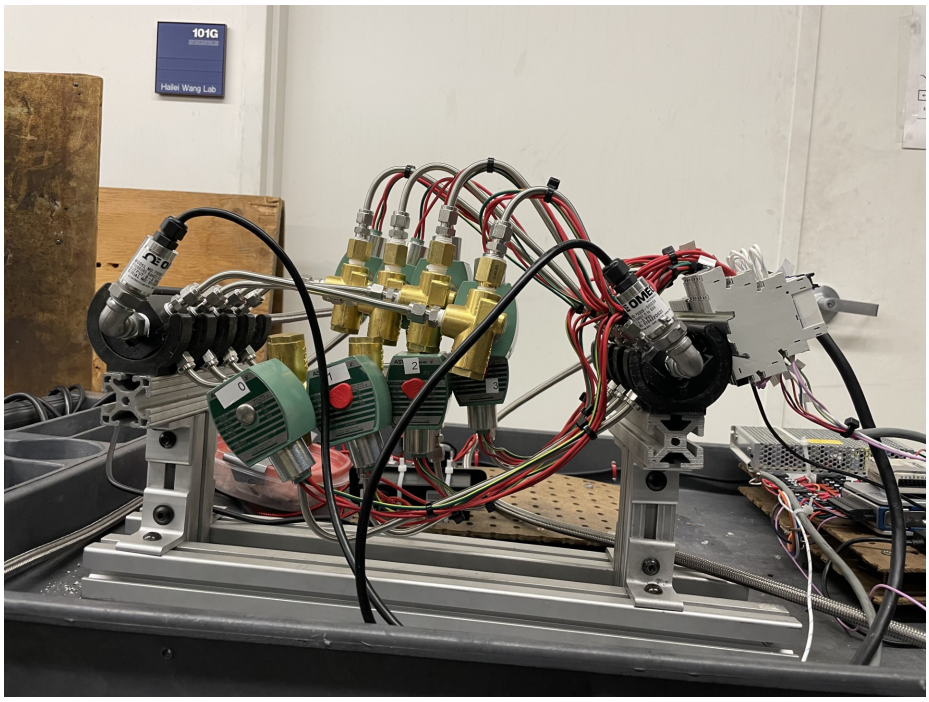

Fig. 4.3: Back view of 8-bit digital throttling valve.

The "8 bits" of the digital valve are all actuated using ASCO 8223G021[1] A/C solenoid operated valve (SOV). The SAAKO rail-mount solid state relays[2] convert the A/C power input to DC control logic. The NI 9472[3] digital output module sends the signal to actuate each valve. The initial estimates for the sizes of flow restriction orifices, found in Table 3.1, produced non-linear throttle patterns during the deep throttle ramp cold-flow test, shown in Fig. 4.4.

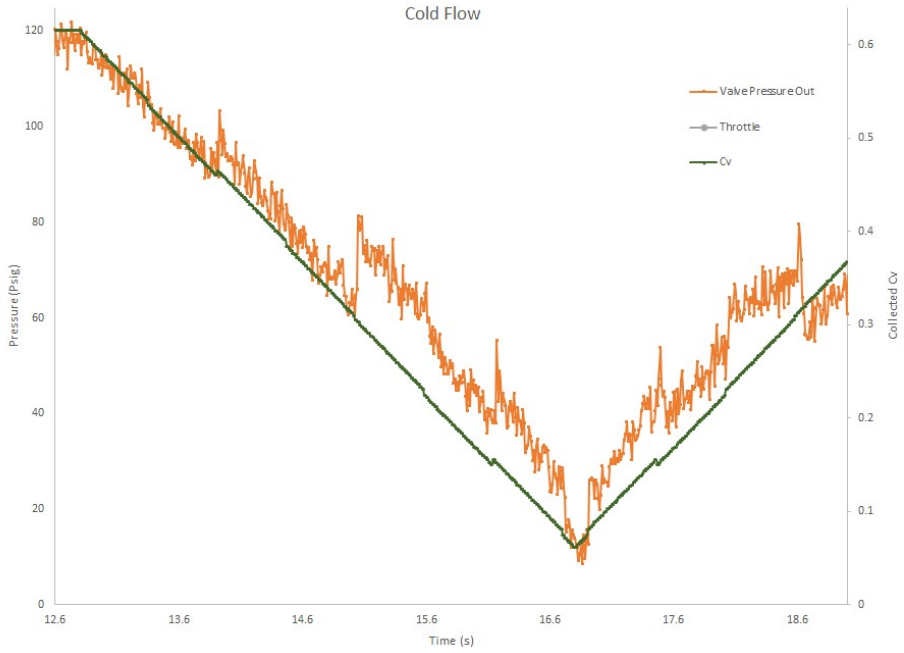

Fig. 4.4: Deep throttle ramp cold-flow test.

To achieve a more linear throttle pattern, the threaded flow control orifices[4] on SOVs 7, 6, and 5 were switched out for orifices that produced smoother throttle patterns, which involved increasing the orifice diameter for SOV 7 and 6 and decreasing the orifice diameter

[1]ASCO, "8223G021 120/60AC 2-Way Brass 1/4 In Solenoid Valve Normally Closed High Pressure", https://valvesandinstruments.com/asco-20369-3043673.html. (accessed: November 21, 2023)

[2]SAAKO, "Mini Ultra-thin Solid State Relay Module Module T41F-3 HF41F-024-012 DC24v 12v 5v", https://www.amazon.com/Ultra-Thin-T41F-3-HF41F-024-012-Connection-Method/dp/B0CBTQT3ZQ?th=1. (accessed: November 21, 2023)

[3]National Instruments, "NI-9472 C Series Digital Module", https://www.ni.com/en-us/shop/model/ni-9472.html, (accessed: November 21, 2023)

[4]Threaded Flow Control Orifice with Brass Body 1/4 NPT Male x Female Adapter, https://www.mcmaster.com/2712T45/. (accessed: November 21, 2023)

attached to SOV 5. The digital valve uses two OMEGA pressure transducers[5], one at the inlet manifold and the other attached onto the outlet manifold, to take valve inlet and outlet pressure data during tests.

4.2 Digital Valve C_v and Mass Flow Calibration

A series of cold-flow tests were performed with compressed gaseous nitrogen (N_2) used as the working fluid through the 8-bit digital throttle valve. This calibration validates the accuracy of the orifice C_v values and the mass flow rate as a function of the digital valve inlet and outlet pressures. The set-up for this calibration is detailed in section 3.3.1. A calibration run for SOV-2 is captured in Fig. 4.5.

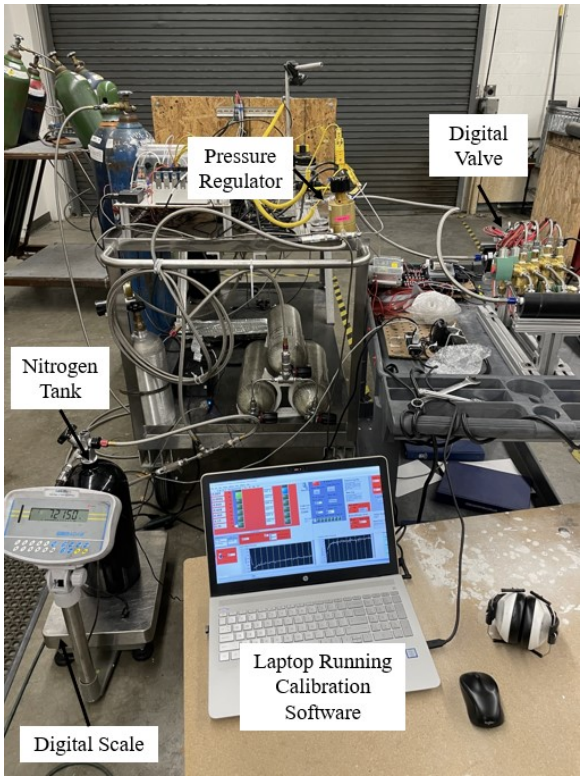

Fig. 4.5: Digital valve calibration test for SOV-2.

[5]General Purpose, Stainless Steel Pressure Transducers, `https://www.omega.com/en-us/pressure-measurement/pressure-transducers/px309/p/PX319-500GI`. (accessed: November 21, 2023)

This calibration data is dropped into a LabVIEW virtual instrument (vi) capable of reading the inlet pressure, outlet pressure, mass, and valve data from the calibration tests to calculate an average C_v value as a function of valve inlet pressure at a 95% confidence level for each SOV. The flow coefficient is computed using either Eq. (4.1) if there choked flow through the flow control orifice or Eq. (4.2) for unchoked flow.

$$C_v = \frac{Q}{816.5}\frac{\sqrt{SG \cdot T}}{P_{in}} \tag{4.1}$$

$$C_v = \frac{Q}{961.7}\left(\sqrt{\frac{SG \cdot T}{P_{in}^2 - P_{out}^2}}\right) \tag{4.2}$$

Figure 4.6 shows an example of calculated flow coefficient as a function of inlet pressure for SOV-3. The presented calibration data, which vents to ambient pressure, used Eq. (4.1) for all the C_v calculations, since the flow was choked through the entire test. Table 4.1 compares the measured C_v values to the expected C_v values. Figure 4.7 shows the comparison between measured and expected C_v values for each SOV, including the total collected C_v value, also shown is the standard deviations.

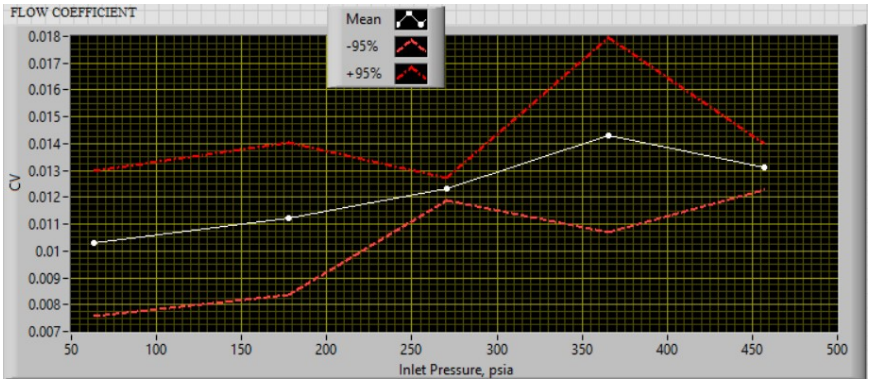

Fig. 4.6: C_v value as a function of valve inlet pressure.

The calibration results show that the tested C_v values of each SOV are about 55% of the nominal values. This means that in the 8-bit digital throttling valve there is significant friction between the piping walls and the GOX, causing a pressure loss. This pressure loss is an irreversible loss of the gas's potential energy. The additional line losses may be

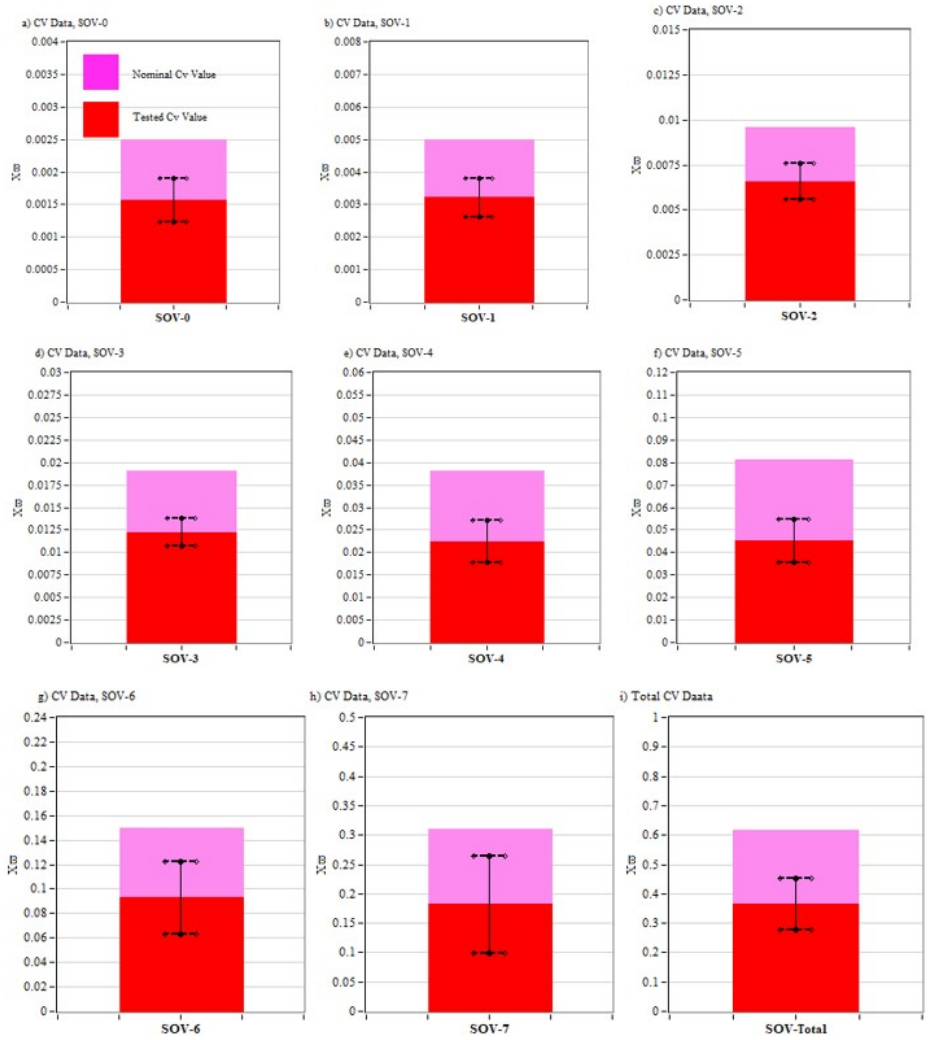

Fig. 4.7: Expected vs. measured C_v value comparisons and standard deviation.

Table 4.1: Final flow restriction orifice sizes and measured C_v value.

Total Collected C_v		> 0.6656	0.3658
SOV #	Orifice Diameter, *in*	Expected C_v Value	Measured C_v Value
SOV-0	0.010	0.0025	0.0016
SOV-1	0.016	0.0055	0.0032
SOV-2	0.021	0.0096	0.0066
SOV-3	0.029	0.0190	0.0123
SOV-4	0.040	0.0360	0.0224
SOV-5	0.055	0.0680	0.0452
SOV-6	0.082	0.1550	0.0929
SOV-7	0.172	> 0.3700	0.1818

attributed to the small piping used in the system, which was 0.493 cm ID pipe. Larger piping in the digital valve might decrease the additional line losses.

4.3 Hybrid Rocket Motor Regression Rate Calibration

The complexities of fuel regression rate of a hybrid rocket motor are described in section 1.2.1. Since the fuel pyrolysis rate is interdependent upon the fuel mass flow, the oxidizer mass flux, and the time-dependent O/F ratio, it usually varies non-linearly as a function of time. Making time-dependent fuel regression rates difficult to measure. Various methods have been proposed to calculate the time-dependent data. One technique developed by Whitmore [37] in 2002 uses the collected oxidizer mass flow and chamber pressure measurements to calculate the time-dependent fuel regression rate.

For this testing campaign, where each hot fire burn exceeds 10 seconds in duration a simple mass-depletion model is used to calculate the fuel regression rate. Taking consumed fuel and oxidizer mass measurements through the duration of each burn to compute the fuel pyrolysis rate is typically accurate time-averaged calculations. For each hot fire test the oxidizer and fuel weights were measured pre- and post-burn to compute the consumed masses, and then divided by the estimated burn time to calculate the time-averaged mass flow rates for both oxidizer and fuel. The time-averaged longitudinal mean regression rate

over the burn duration is calculated in Eq. (4.3) as

$$\bar{\dot{r}}_L = \frac{\Delta M_{fuel}/t_{burn}}{2\pi \cdot \rho_{fuel} \cdot \left[\frac{\bar{r}_L(t_{burn})+r_0}{2}\right] \cdot L} \tag{4.3}$$

Where $\bar{r}_L(t_{burn})$ is the mean measured fuel port radius at the end of the burn. The time-dependent fuel port radius is computed in Eq. (4.4)

$$\bar{r}_L(t) = r_0 + \bar{\dot{r}}_L \cdot t \tag{4.4}$$

To quantify how the fuel regression rate varies over time for the 98mm ABS/GOX hybrid rocket motor, a set of 3 100% constant thrust burns were performed on a single fresh ABS fuel grain. To calculate ΔM_{fuel}, the pre- and post-burn fuel mass was taken for each test. Plotted for each test is first the thrust as a function of time. One thrust curve is measured directly from the load cell and the other is calculated from the chamber pressure using de Laval flow equations. The next plot shows the oxidizer, total, and fuel mass flow rates as a function of time. The oxidizer and fuel mass flow rates are calculated using the methods described in sections 3.1.4 and 1.2.4, respectively. The total mass flow is calculated in Eq. (4.5) as

$$\dot{m}_{tot} = \dot{m}_{ox} + \dot{m}_{fuel} \tag{4.5}$$

The final plot displays the fuel regression rate, calculated using the method described above and shown in Eq. (4.3), as a function of oxidizer mass flux. Power-law curve fits are plotted as well to empirically determine the constants a and n. Fig. 4.8 shows the three plots discussed above for each of the regression rate calibration tests. Notice that the thrust, total mass flow, and fuel mass flow rates all vary significantly for the first burn, moderately for the second burn, and remain relatively constant for the third burn, even though the oxidizer mass flow stays constant and steady through the duration of each burn. Based on the discussion at the end of section 1.2.4, this behavior is indicative of fuel rich motor combustion, and of a burn exponent, n, of less than one-half.

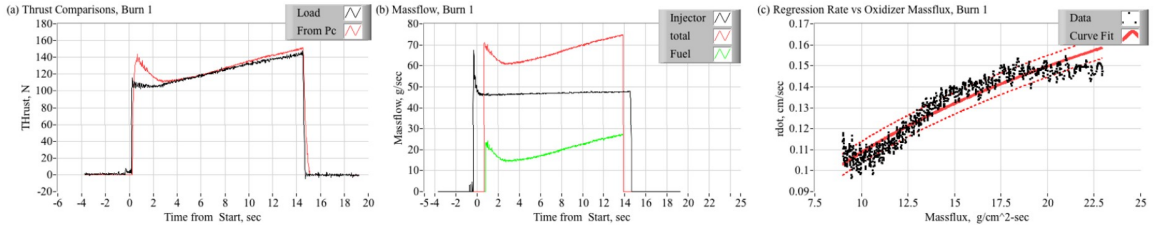

(a) Regression burn 1

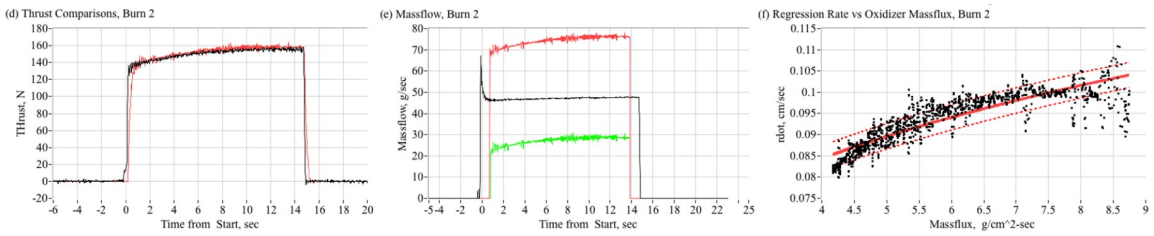

(b) Regression burn 2

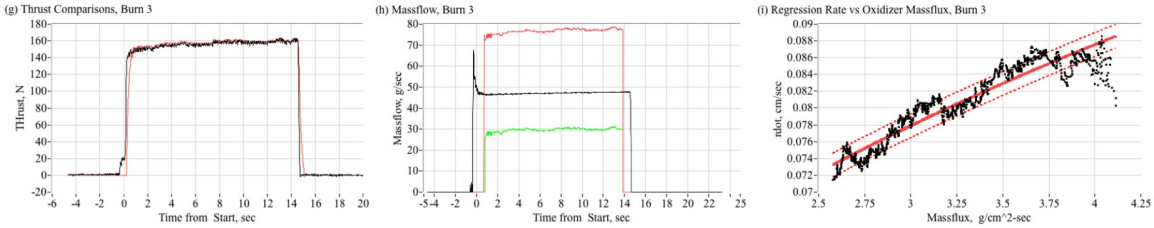

(c) Regression burn 3

Fig. 4.8: Hot fire data for steady-state fuel regression rate tests.

To get an idea of the cumulative regression rate, the fuel regression rate data from all three burns are combined and plotted in Fig. 4.9, along with a cumulative Power-law curve fit to determine cumulative constants a and n.

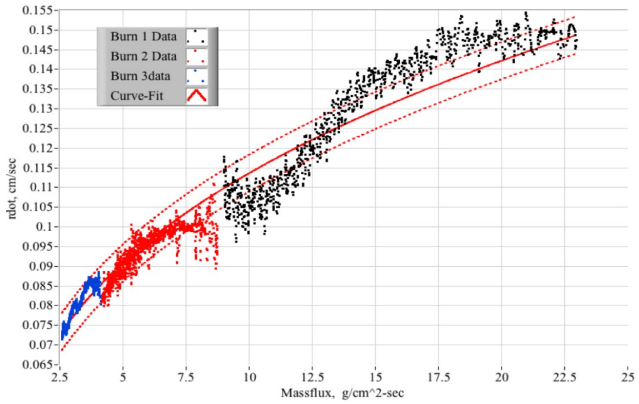

Fig. 4.9: Combined fuel regression rates for each calibration test.

Table 4.2 summarizes the curve-fit coefficients for the three fuel regression rate calibration burns and the combined data. The estimated burn exponents all fall in the negative O/F ratio shift range, which agree well with the burn behavior for the fuel regression rate calibration tests. The last row in the table displays the mean values for the curve-fit coefficients, which will be dropped into Eq. (1.7) for calculating the fuel regression rate in the analytical model.

Table 4.2: Fuel regression rate calibration Power-law curve-fit coefficient summary.

Throttle Level	100%		
Curve-Fit Coefficients	a, $\frac{cm/s}{(g/cm^2-s)^n}$	n	RMS Fit Error, cm/s
Burn 1	0.0043	0.2836	$\pm$0.0225
Burn 2	0.00475	0.3796	$\pm$0.0155
Burn 3	0.00625	0.4065	$\pm$0.0161
Combined Data	0.00506	0.3239	$\pm$0.0121
Mean Values	0.0046	0.3320	$\pm$0.0117

4.4 Deep Throttle Ramp Test and Analysis

A deep throttle ramp test was performed to identify how the motor responds linear deep-throttling, as shown in Fig. 3.11a. The commanded throttle pattern starts at 100% for 2 seconds after the run valve opens, then ramps down linearly to 10% throttle for 3 seconds, ramps back up to 100% throttle again for 3 seconds, and finally runs at 100% throttle for an additional 2 seconds. Making for a total commanded burn time of 10 seconds. This burn featured a fresh fuel grain.

Figure 4.10 plots the commanded and measured thrust, injector and chamber pressures, mass flows, digital valve pressures, and O/F ratio over the duration of the burn. In Fig. 4.10a, the commanded throttle profile is plotted against the actual thrust response measured from the load cell. The actual thrust response does show a linear response, which is a result of the correct orifice sizing on each SOV. Compared to the commanded value, the actual thrust shows latency and roll off issues. The next plot, Fig. 4.10b, compares the thrust measured from the load cell and thrust calculated from chamber pressure measurements. The two curves agree well, verifying the accuracy of the data sensors. Notice, both curves seem to increase over time and end up at a higher thrust than at the beginning of the burn. The 8-bit digital valve exhibits a turndown ratio of about 4:1 for this test.

The following plot, Fig 4.10c, compares the measured chamber and injector pressures. Notice that the system remained choked at the injector during the test, a good sign to ensure there is no pressure feedback coupling. Figure 4.10d shows the oxidizer mass flow through the injector, the fuel mass flow, and total mass flow. As expected from the regression rate calibration tests, even though the oxidizer mass flow through the injector follows the throttle pattern, the fuel mass flow gradually increases through the burn. The maximum oxidizer mass flow rate achieved is about 40 g/s. The digital valve inlet and outlet pressures along with pressure at the injector, labeled as $P1$, $P2$, and PIj, respectively, are shown in Fig. 4.10e. Notice the valve inlet pressure curve showing an inverse correlation to the outlet pressure curve, which signifies that the system remains unchoked through the digital valve. This causes some pressure coupling upstream, but the digital valve is still able to provide an

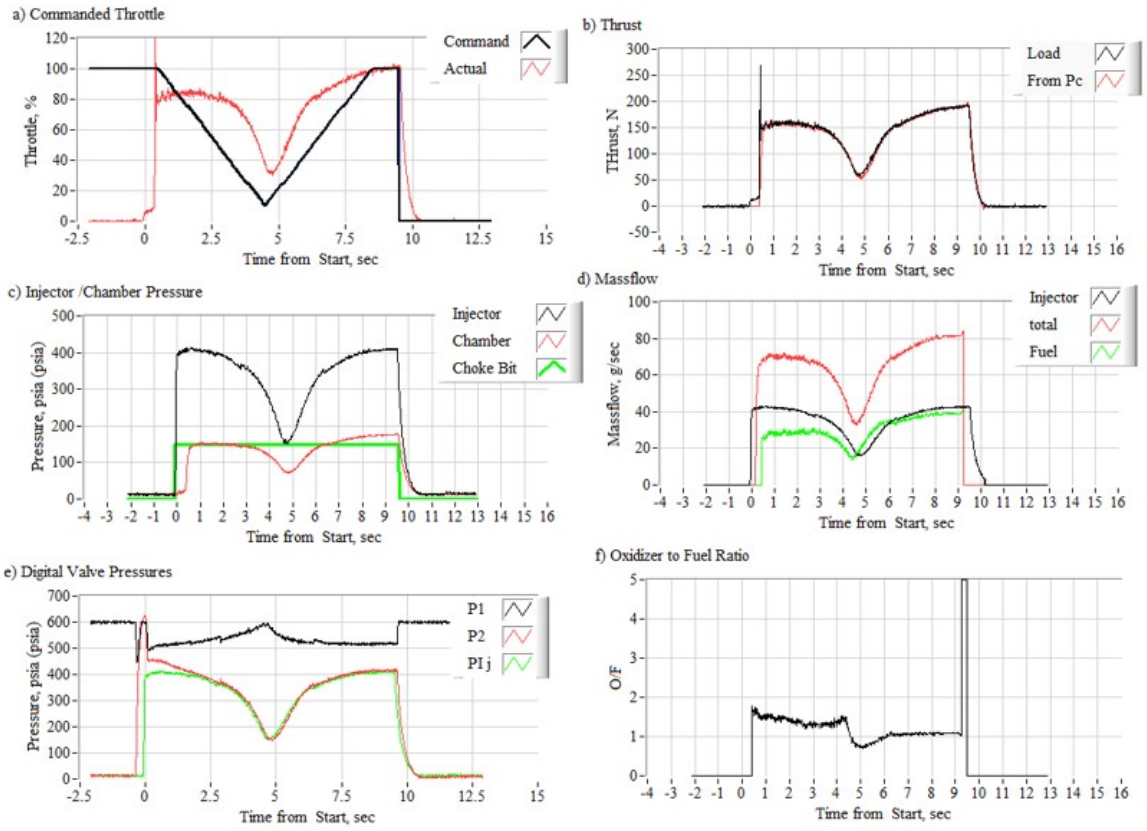

Fig. 4.10: Deep throttle ramp test performance data.

accurate pressure output according to the throttle profile. The O/F ratio time-history, in Fig. 4.10f, confirms the negative O/F ratio shift behavior that the previous plots revealed. This agrees well with the analytical model's predictions. To further analyze this O/F ratio shift, the next test uses this same fuel grain.

4.5 Deep Throttle Multi-Step Boxcar Test and Analysis

A test was performed with the deep throttle multi-step boxcar commanded throttle pattern, as shown in Fig. 3.11b. The duty cycle throttles down from 100% to 60%, 100% to 50%, 100% to 30%, and 100% to 20% before throttling back up to 100% at 1.25 second intervals. This throttle pattern is aimed to test the responsiveness of the 8-bit digital valve to instantaneous changes in commanded throttle percentages. This burn was performed using the same fuel grain as the deep throttle ramp test in section 4.4 to further examine the effects of O/F shift on hybrid rocket motor performance. Figure 4.11 presents the results of the multi-step boxcar tests as time-history plots of 6 key parameters; a) commanded thrust, b) thrust measurements, c) injector and chamber pressures, d) oxidizer, total, and fuel mass flow rates, e) digital valve pressures, and f) O/F ratio.

Again, the actual thrust response of the motor shows difficulty keeping up with the instantaneous changes in throttle command, which shows up as rounding off and latency of the data. Setting the steady-state throttle intervals to higher values to give the motor more time to respond may clean the data up. The thrust comparison plot shows that the combustion chamber experienced an even higher delay in response time than the thrust measured from the load cell. Although, this behavior is indicative of delays during the complex combustion of hybrid rocket motors, not of the digital valve effect on the system. As shown in the digital valve pressure plot, in Fig. 4.11e, the outlet pressure does a decent job at tracking the commanded throttle profile, apart from the response latency in the data of course. During this test, the digital valve achieves a maximum oxidizer mass flow rate of about 55 g/s.

Generally, the roll off of the actual injector and chamber pressure peaks, in Fig. 4.11c match that of the thrust peaks shown in Fig.4.11b. In contrast, even though the peaks of

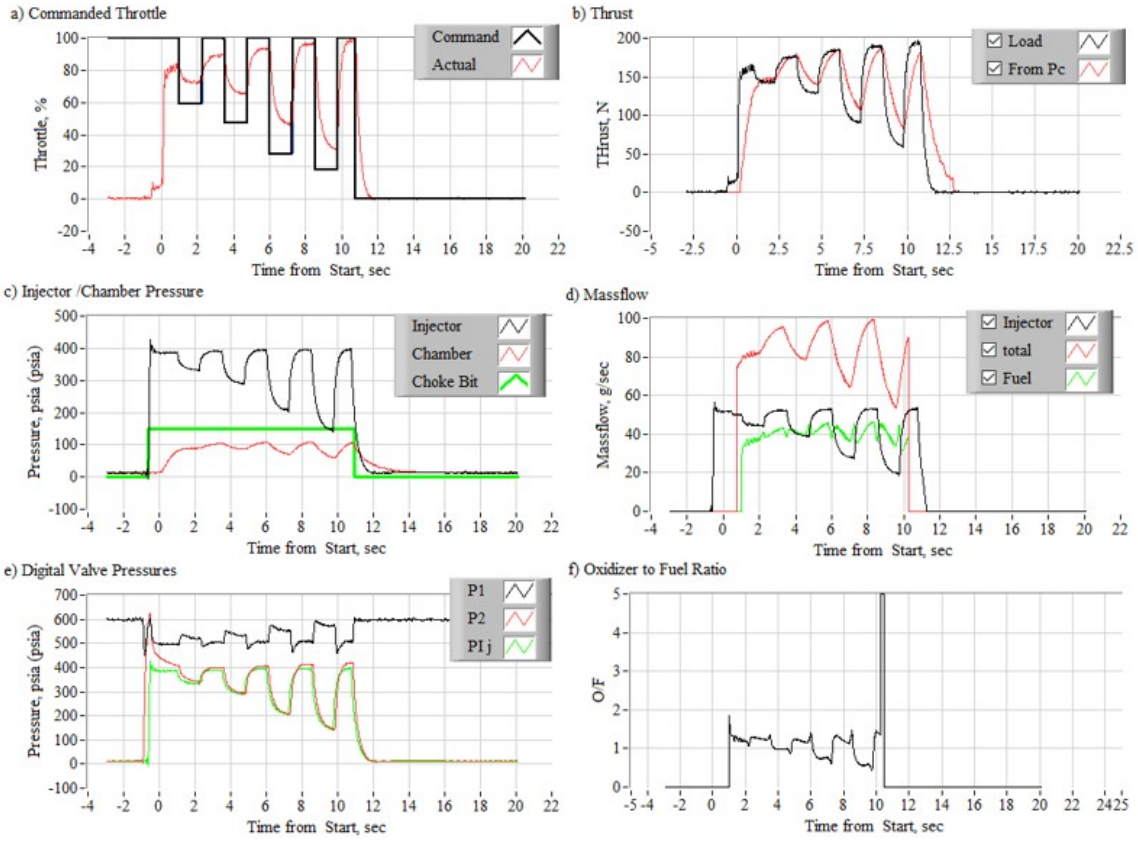

Fig. 4.11: Deep throttle multi-step boxcar test 1 performance data.

oxidizer mass flow rate, in Fig. 4.11d, remain close to constant; the peaks of thrust and fuel mass flow rate seem to grow slightly with time. While the peaks of O/F ratio, in Fig.4.11f, seems to remain relatively constant, only a slight negative O/F shift is noticeable. The large spike shown on this curve is only an artifact of the data collection being terminated preemptively and does not reflect an actual jump in O/F ratio. The O/F ratio curves between burn 1 and burn 2 with this fuel grain exhibit significantly different behavior.

To provide data that demonstrates this behavior more clearly, two additional tests of the deep throttle multi-step boxcar profile were performed. The first test utilizes a fresh fuel grain, while the second test uses the same fuel grain again. The performance data for the first test is shown in Fig. 4.12a and the second in Fig. 4.12b. By comparing two tests of the same throttle profile, the effects of negative O/F ratio shift are much more obvious. During these burns, the digital valve was shown to be capable of achieving a turndown ratio of about 40:1 and oxidizer mass flow rates of about 60 g/s. Even though the peaks of oxidizer mass flow curves for both burns remain nearly constant, the first burn time-histories of thrust, fuel mass flow, and O/F ratio exhibit significantly different behaviors compared to the second burn. The peaks of the thrust and the fuel mass flow rate curves of the fist burn gradually increase with time, while the same peaks show almost no increase over time during the second burn. Comparing the O/F ratio plots of the two burns shows that the observed negative shift in O/F ratio seems to be diminishing over fuel grain burn time. It is worth noting that the analytical model accurately predicts these trends, verifying that these trends are not a result of throttling, but of complex behaviors of hybrid rocket motor combustion. Section 4.7 aims to analyze the reason for this behavior.

4.6 Sine Wave Throttle Test and Analysis

Finally, the rapid response rate, and deep throttle capabilities of the 8-bit digital valve system was put to the test using a sine wave throttle profile at command frequency of 0.5 Hz. The commanded throttle profile achieves 4 full sine waves within a burn time of 10 seconds. Figure 4.13 shows the results of the sine wave throttle test. The 6 performance parameters plotted as a function of time are a) commanded vs actual thrust, b) thrust comparisons, c)

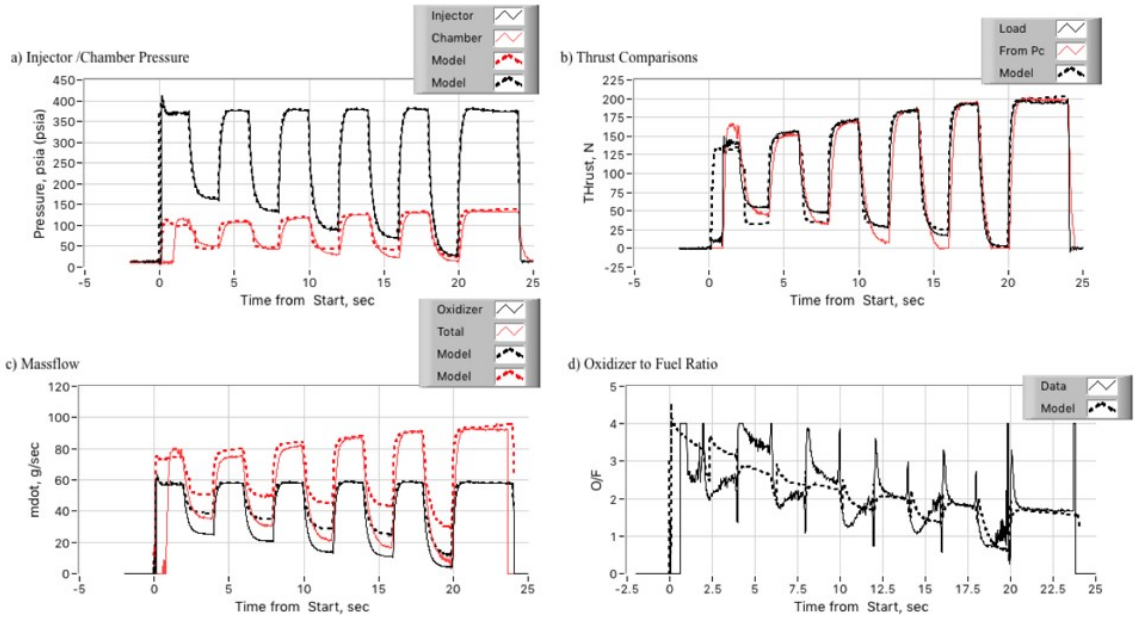

(a) Multi-step boxcar throttle burn 1

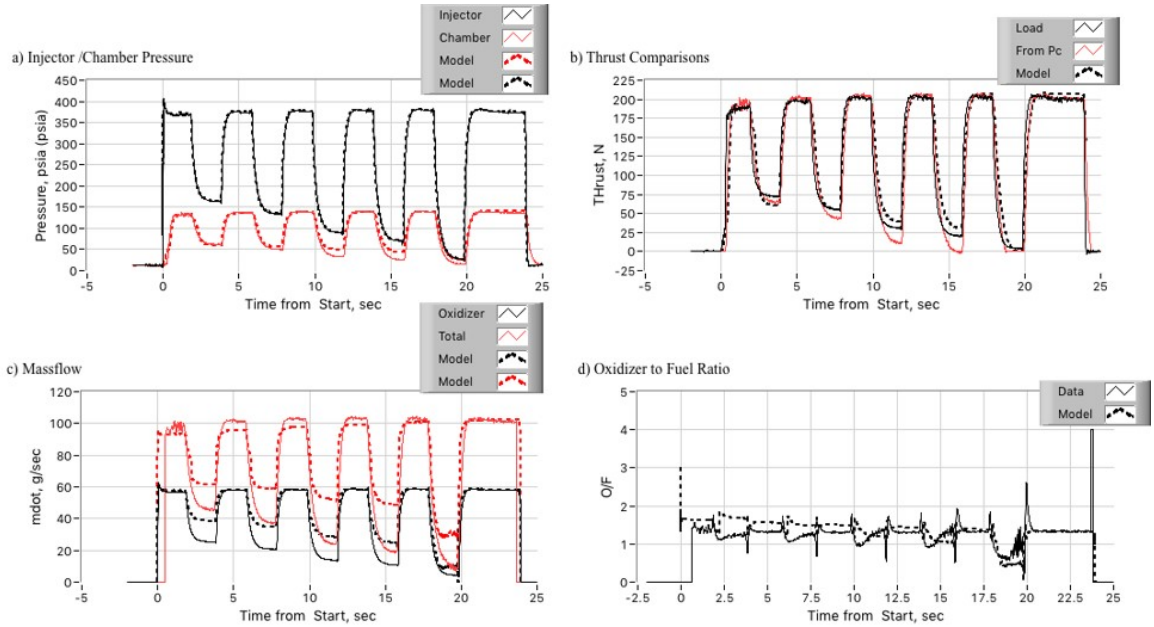

(b) Multi-step boxcar throttle burn 2

Fig. 4.12: Deep throttle multi-step boxcar test 2 performance data.

injector and chamber pressures, d) mass flow of the oxidizer, fuel, and combined, e) 8-bit digital valve pressures, and d) O/F ratio.

Notice that the actual thrust response is somewhat damped compared to the commanded throttle pattern, shown in Fig. 4.13a. In other words, the digital valve cannot precisely keep up with the commanded throttle 0.5 Hz sine wave. Note the pressure feedback coupling occurring through the orifices on each SOV, observed in Fig. 4.13e. This feed pressure coupling may also contribute to some of the observed response distortions compared to the commanded throttle profile. Once again, the time-history plots of thrust, fuel mass flow, and O/F ratio all exhibit the effects of negative O/F ratio shift. However, the performance effects do seem to be of lesser magnitude.

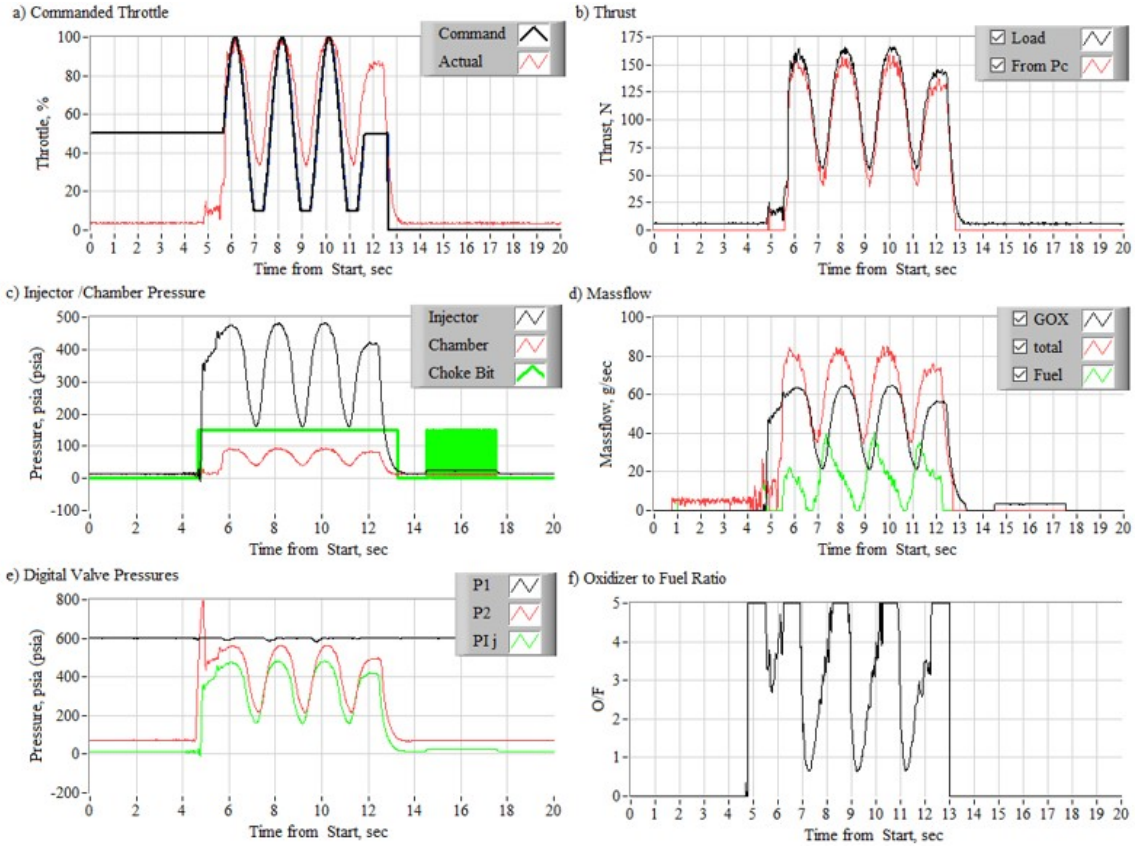

Fig. 4.13: Sine wave throttle test performance data.

4.7 Negative O/F Ratio Shift Analysis

To provide analysis and an explanation for the negative O/F ratio shift behavior and its effect on hybrid rocket motor performance, observed in sections 4.4, 4.5, and 4.6, a simple linear analysis is demonstrated. The O/F ratio calculation, in Eq. (1.9), is expanded for a cylindrical fuel port, shown in Eq. (4.6)

$$\begin{aligned} O/F &= \frac{\dot{m}_{ox}}{\dot{m}_{fuel}} \\ &= \frac{\dot{m}_{ox}}{\rho_{fuel} \cdot A_{burn} \cdot \dot{r}} \\ &= \frac{\dot{m}_{ox}}{\rho_{fuel} \cdot (2\pi \cdot r \cdot L)\dot{r}} \end{aligned} \tag{4.6}$$

Substituting the Marxman Law for regression rate, in Eq. (1.7) and allowing $m \approx n-1$ gives Eq. (4.7)

$$\begin{aligned} &= \frac{\dot{m}_{ox}}{\rho_{fuel} \cdot (2\pi \cdot r \cdot L) \cdot (a \cdot G_{ox}^{n} \cdot L^{m})} \\ &= \frac{\dot{m}_{ox}}{\rho_{fuel} \cdot (2\pi \cdot r \cdot L) \cdot a \left(\frac{\dot{m}_{ox}}{\pi \cdot r^2}\right)^{n} \cdot L^{m}} \\ &= \frac{\dot{m}_{ox}^{1-n} \cdot r^{2n-1}}{\rho_{fuel} \cdot (2\pi^{1-n} \cdot a) L^{1+m}} \end{aligned}$$

$$O/F = \frac{\dot{m}_{ox}^{1-n} \cdot r^{2n-1}}{\rho_{fuel} \cdot (2\pi^{1-n} \cdot a) L^{n}} \tag{4.7}$$

From this expansion, an equation for O/F ratio shift is developed in Eq. (4.8) by calculating the derivative of O/F ratio with respect to time

$$\begin{aligned} \frac{\partial (O/F_{(t)})}{\partial t} &= \left(\frac{\dot{m}_{ox}^{1-n}}{\rho_{fuel} \cdot (2\pi^{1-n} \cdot a) L^{n}}\right) \frac{\partial \left(r^{2n-1}\right)}{\partial t} \\ &= \left(\frac{\dot{m}_{ox}^{1-n}}{\rho_{fuel} \cdot (2\pi^{1-n} \cdot a) L^{n}}\right) \left((2n-1) \cdot r^{2n-2} \cdot \dot{r}\right) \\ &= \left(\frac{(2n-1) \cdot \dot{m}_{ox}^{1-n}}{\rho_{fuel} \cdot (2\pi^{1-n} \cdot a) L^{n}}\right) \cdot r^{2(n-1)} \cdot \left[a \left(\frac{\dot{m}_{ox}}{\pi r^2}\right)^{n} \cdot L^{n-1}\right] \\ &= \left(\frac{(2n-1) \cdot \dot{m}_{ox}}{\rho_{fuel} \cdot (2\pi \cdot r^2) L}\right) \end{aligned}$$

$$\implies \frac{\partial(O/F_{(t)})}{\partial t} = \left(\frac{(2n-1)\cdot \dot{m}_{ox}}{\rho_{fuel}\cdot v_{port}}\right) \tag{4.8}$$

Substituting the mean burn exponent, $n = 0.332$, found in table 4.2 into both Eqs. (4.7) and (4.8) produces Eq. (4.9)

$$\implies n = 0.332$$

$$(a)\ O/F_{(t)} = \frac{\dot{m}_{ox}^{0.668}}{\rho_{fuel}\cdot(2\pi^{0.668}\cdot a)\cdot L^{0.332}\cdot r_{(t)}^{0.336}}$$

$$(b)\ \frac{\partial(O/F_{(t)})}{\partial t} = -0.336\cdot\left(\frac{\dot{m}_{ox}}{\rho_{fuel}\cdot v_{port_{(t)}}}\right) \tag{4.9}$$

Equation (4.9a) shows that the O/F ratio decreases with time as the fuel port burns and fuel port radius increases. However, Eq. (4.9b) shows that simultaneously the rate of decrease will diminish with time as the fuel port radius and internal volume grow during the burn. This predicted behavior matches the observed behaviors of the presented time-history plots of Figs. 4.10, 4.11, 4.12 and 4.13. The behavior becomes even more obvious in Fig. 4.14 which plots the O/F shift rate of the first deep ramp and multi-step throttle burns. The O/F ratio shift rate drops by a factor of about 3 from burn 1 to burn 2. As the fuel port diameter grows with time, the intensity of O/F ratio shift of the motor decreases. The observed increasing thrust trend is not due to throttling, but instead is caused by the negative, or fuel-rich, O/F shift in the hybrid rocket motor.

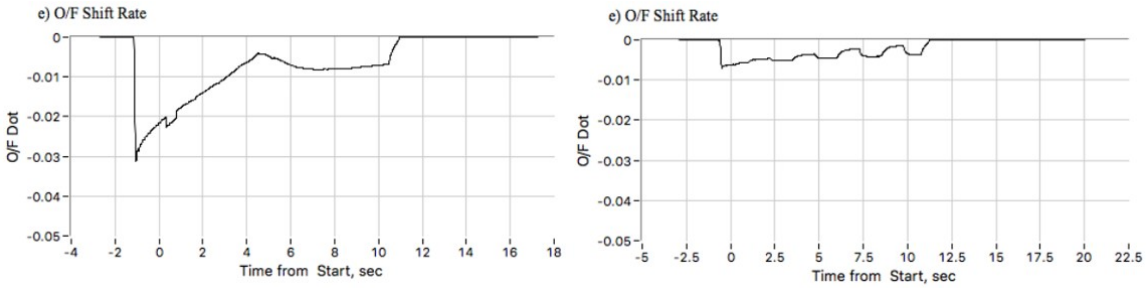

Fig. 4.14: O/F ratio shift rate as a function of time for hot fire burn 1 and 2.

4.8 Frequency Response Analysis

As shown in sections 4.4 and 4.5 the commanded thrust versus actual thrust plots displayed significant latency and roll off. This section investigates the source of this loss in response fidelity, by performing a frequency analysis. The frequency analysis data is generated by using a LabVIEW vi to bring in a single signal sampled from a hot fire test. The number of elements in the sampled signal is then interpolated to be a power of two and then the output is zero padded. The modified signal is then run through a DFT implemented as a power of two FFT algorithm to transform the signal from the time domain into the frequency domain and generates a frequency spectrum. The vi then breaks the frequency spectra into two components, the magnitude and phase, and plots those components on the front panel. Figure 4.15 gives an example of the vi front panel for an 8-bit commanded throttle signal.

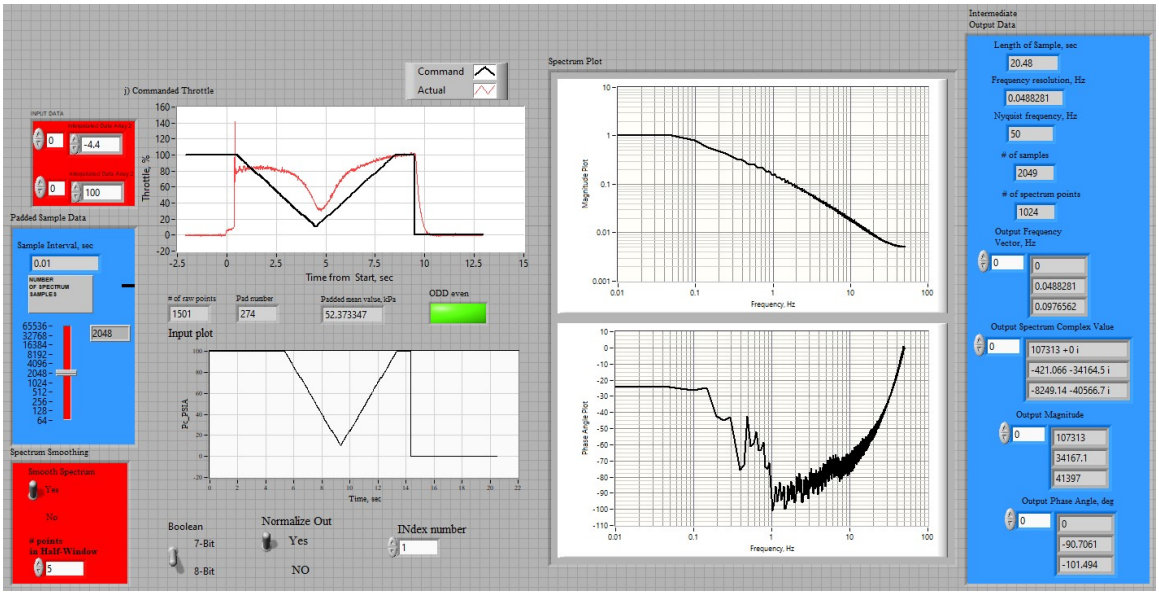

Fig. 4.15: Frequency spectra LabVIEW vi front panel.

Using a separate vi, the magnitude and phase components of the signal are scaled to account for magnitude differences and then plotted with other magnitude and phase components of another sampled signal for comparison purposes. The frequency analysis data

is generated using this method. To develop a good understanding of the system frequency response, the following frequency spectra are compared; 1) digital valve inlet and outlet pressures, 2) digital valve outlet and injector pressures, 3) injector and chamber pressures and 4) chamber pressure, thrust measured from the load cell, and 8-bit throttle command. The fourth comparison plot represents the end-to-end system frequency response. Figure 4.16 shows the location on the P&ID where each of these spectra are sampled from, the annotated values correspond to the list above. This frequency analysis is performed for both the deep throttle ramp and multi-step boxcar hot fire tests.

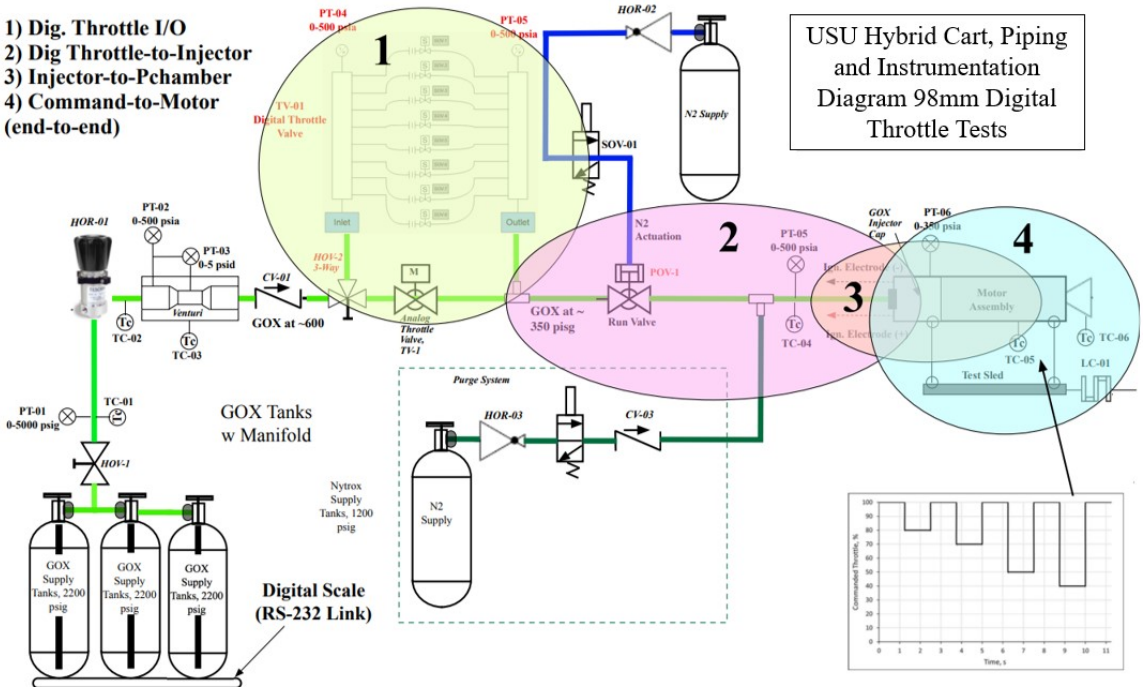

Fig. 4.16: Sample location of resulting spectra on the P&ID.

The time-history plots shown in Fig. 4.10 for the deep ramp throttle test and in Fig. 4.11 for the deep throttle multi-step boxcar test correspond to the following frequency spectra plots in Figs. 4.17 and 4.19.

4.8.1 Deep Throttle Ramp Frequency Response Analysis

Figure 4.17a shows the digital valve frequency response, which path corresponds to label 1 in Fig. 4.16. The black curve represents the transform of the inlet pressure, the red curve represents the transform of the outlet pressure, and the blue curve represents the transform of the commanded throttle. Notice on the spectrum magnitude plot the digital valve outlet pressure rolls off towards a lower magnitude compared to the commanded throttle around 1 Hz. This attenuation caused by the digital valve could explain the data rounding shown in Fig. 4.10a.

Also notice on the spectrum phase angle plot the digital valve outlet pressure curve exhibits a higher phase angle than the commanded throttle curve, which is equivalent of a phase lag, or in other words a timing lag. This phase lag shows up in both Figs. 4.10a and 4.10e, so the digital valve may be a contributing factor to the observed latency as well. The oscillations that show up in the digital valve inlet and outlet transforms are representative of the harmonics that are introduced in the digital valve. These reflections from one side of the valve piping to the other are like the harmonics that exist in organ pipes. Finally, the flat line behavior of the digital valve pressure transforms around 12-15 Hz reveals the frequency response limit of the digital valve.

Figure 4.17b shows the frequency response of the path corresponding to label 2 in Fig. 4.16. Where the red curve represents the transform of the injector pressure, and the black curve represents the digital valve outlet pressure. Observe how there exists almost no phase latency between these two transforms. That means even though the piping that connects the digital valve outlet to the injector on the forward end of the motor is of considerable length for the oxidizer to travel, it does not contribute to the latency in the system response. The injector pressure transform does not display the same harmonic oscillations apparent in the digital valve, which shows the harmonic response has damped before entering the motor due to piping.

Figure 4.17c represents the frequency response of the hybrid rocket motor itself, which corresponds to the path labeled 3 in Fig. 4.16. Where the black curve represents the

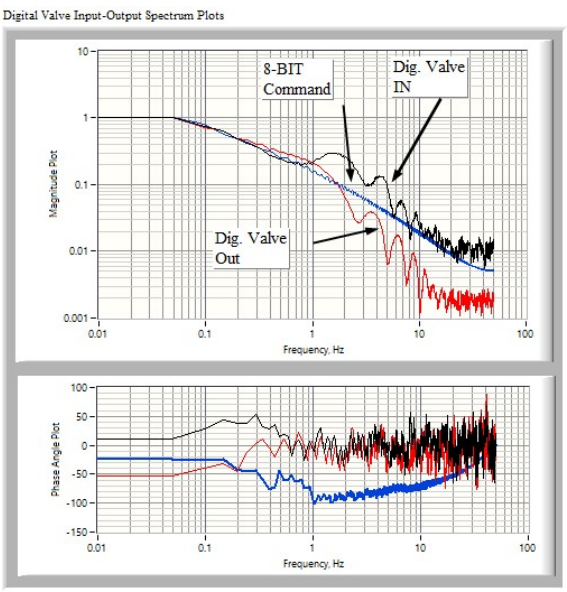

(a) Spectrum 1

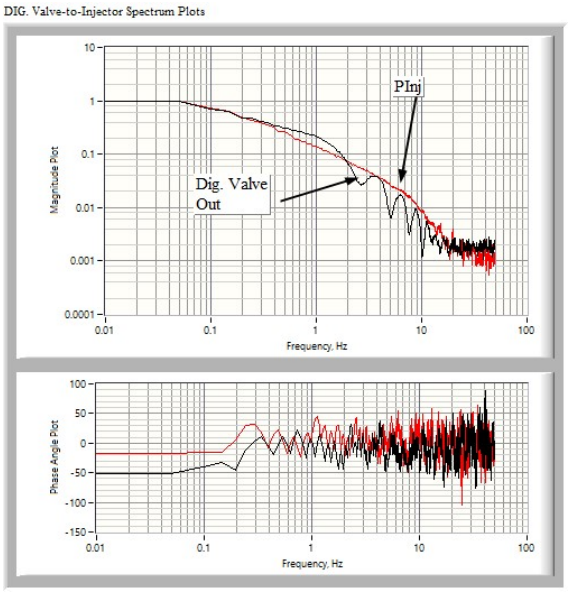

(b) Spectrum 2

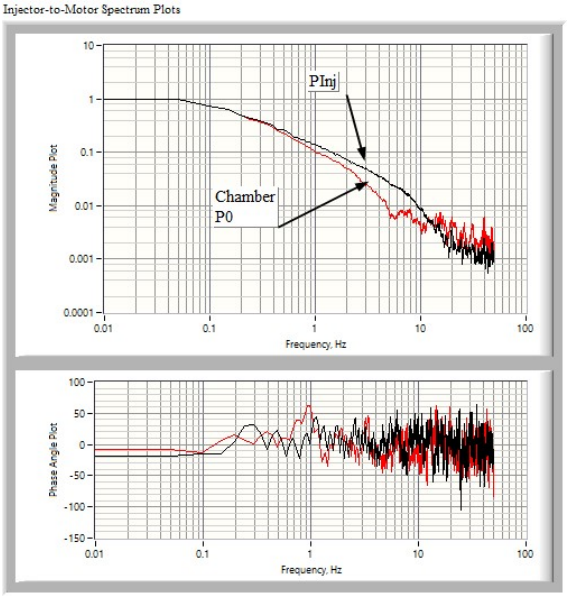

(c) Spectrum 3

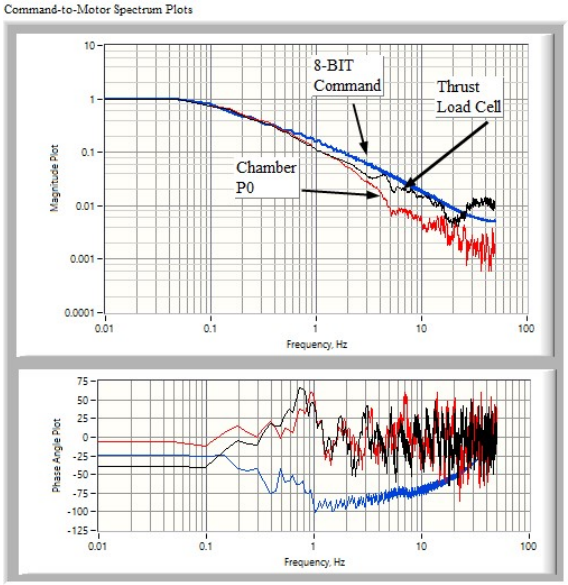

(d) Spectrum 4

Fig. 4.17: Frequency response during deep throttle ramp test.

transform of the injector pressure signal and the red curve represents the transform of the chamber pressure signal. Notice the phase angle lag in the chamber pressure transform, signifying a slight delay in motor combustion response to the injection of oxidizer.

Figure 4.17d represents the end-to-end system frequency response, or how the hybrid rocket motor is responding to the commanded throttle value. This path corresponds to label 4 in Fig. 4.16. The blue curve represents the transform of the commanded throttle signal, the black curve represents the transform of the thrust measurements from the load cell, and the red curve represents the transform of the chamber pressure signal. Again, pressure and thrust data can be compared on the same plot because both transforms have been scaled to account for magnitude differences. The hump on the thrust transform around 3 Hz is likely a result of resonating behavior in the thrust stand since that same peak is not shown in the chamber pressure transform. Notice that the spectrum magnitude of all three transforms track closely until about 1 Hz. This means that the digital throttle valve can respond accurately to changes in throttle command on the order of about 1 second, if the valve is commanded to operate any faster, that is when latency and roll off occur within the system, which is represented in Fig. 4.10a

Before all 8 SOVs were connected, an initial deep throttle ramp test was conducted by the USU PRL to check digital valve functionality with only 7 SOVs. Comparing the frequency response of the 7-bit deep throttle ramp data to the 8-bit deep throttle ramp data yields interesting results. Figure 4.18 presents the end-to-end system frequency response of the 8-bit digital valve, Fig. 4.18a, and the 7-bit digital valve, Fig. 4.18b. The biggest difference between the 8-bit control and 7-bit control is how quickly the 7-bit transform of the chamber pressure drops off and becomes saturated when compared to the 8-bit transform. This proves that the 8-bit digital valve has a better response fidelity, which is most likely due to the addition of the SOV equipped with the smallest diameter flow restriction orifice attached downstream.

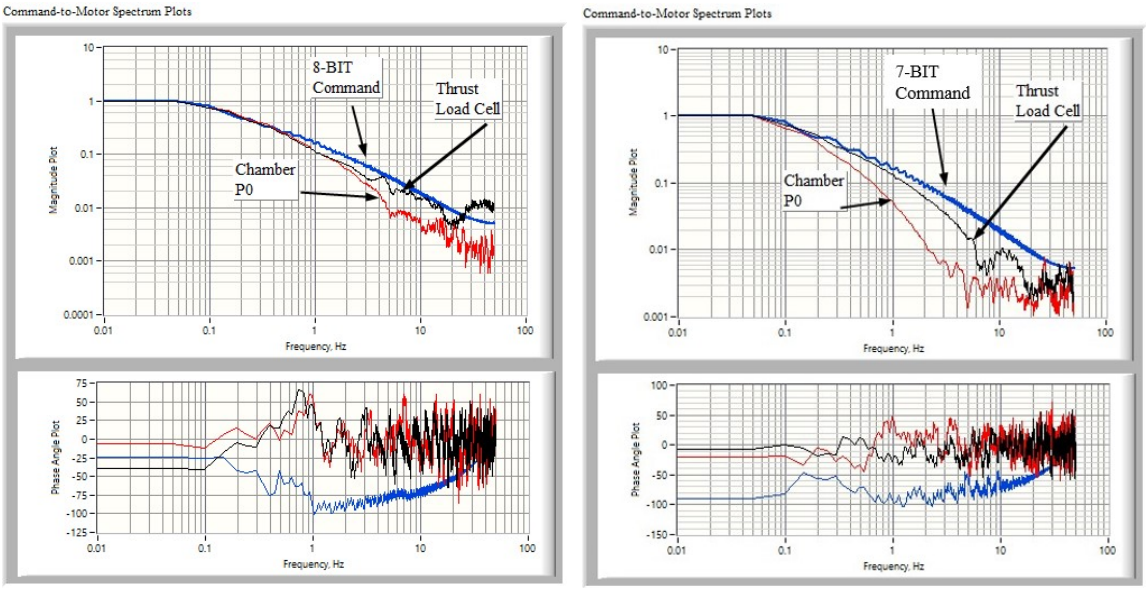

(a) 8-bit control (b) 7-bit control

Fig. 4.18: Frequency response comparison of deep throttle ramp tests.

4.8.2 Deep Throttle Multi-Step Boxcar Frequency Response Analysis

Figure 4.19 presents the same frequency response data as section 4.8.1 but analyzes the deep throttle multi-step boxcar test instead. The data shown in Figs. 4.17 and 4.19 exactly correlate to one another, so the prior frequency response analysis goes into much more detail. However, there are a few valuable items to point out for this frequency response analysis. The harmonic behavior of the digital valve is intensified by this multi-step throttle pattern and even causes some harmonics at the injector as shown by Figs. 4.19a, 4.19b, and 4.19c.

Figure 4.19d, which represents the system frequency response for the deep throttle multi-step boxcar test, agrees well with the system frequency response for the deep throttle ramp test in that the spectrum magnitude of all three transforms track closely until around 1 Hz. This verifies that 8-bit digital valve exact response fidelity is up to 1 Hz and does a decent job at tracking the commanded throttle up to about 10-11 Hz. The flat line frequency response that all four plots exhibit around 12 Hz is likely due to Nyquist frequency limitation. The driving software, and digital interface components cannot operate at a

higher sampling rate and may attribute to some of the observed latency and attenuation roll off.

4.9 Future Work

The hot fire testing campaign in this thesis relies on open-loop throttle control where a prescribed throttle profile is fed into the control software and the 8-bit digital valve responds by actuating the appropriate SOVs to alter the oxidizer flow during a burn. This throttling technology opens the possibility of developing a feed-forward control scheme that allows the system to overcome observed system latencies, commanded throttle distortions, and O/F shift in the motor. One approach to demonstrate this concept would be to use the growing thrust peaks shown in Fig. 4.11a, caused by the negative O/F ratio shift, to scale the commanded deep throttle multi-step boxcar profile. The resulting scaled throttle command generates a motor response that diminishes over time, resulting in a uniform thrust profile. This example does require the system to have excess mass flow capacity to scale the throttle command but illustrates the application.

Currently, in the USU PRL a testing campaign is underway that aims to understand how a hybrid rocket motor responds to manipulation of combustion gases via oxidizer injection with a digital throttle valve. The main goal of this project is to develop an automatic O/F ratio shift compensation motor with a control law that is informed by the experimental data. Having the ability to compensate for O/F shift in hybrid rocket motors has the potential to eliminate the significant obstacles, described in section 1.2, that keep hybrids from being used in a wide range of spaceflight applications. The digital throttling valve technology is a key component of this project and clearly this topic is rich for future research.

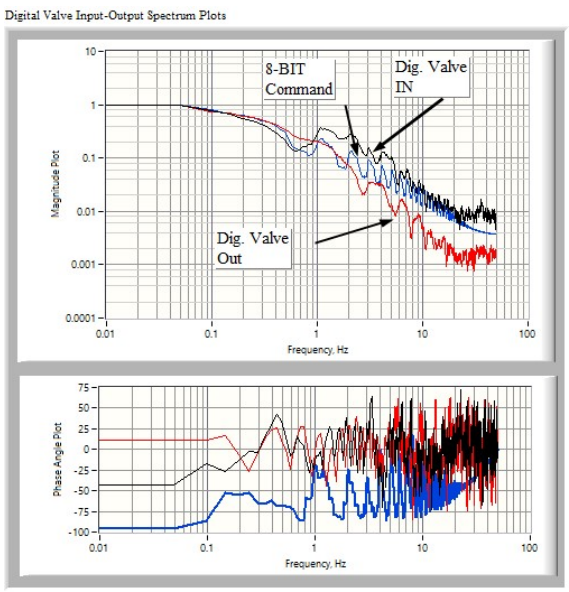

(a) Spectrum 1

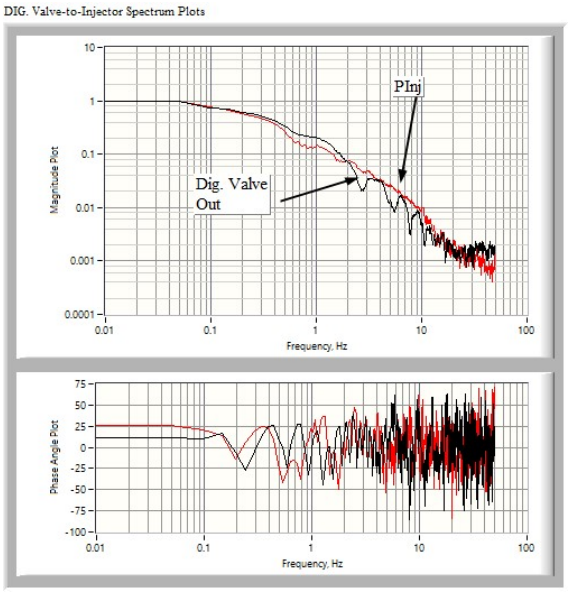

(b) Spectrum 2

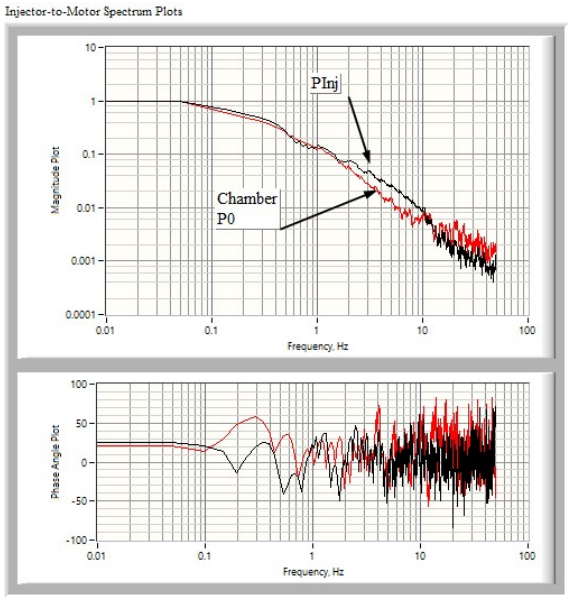

(c) Spectrum 3

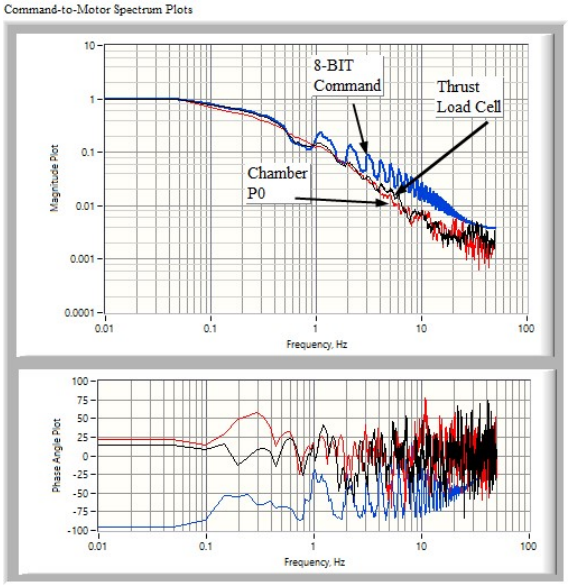

(d) Spectrum 4

Fig. 4.19: Frequency response during deep throttle multi-step boxcar test.

CHAPTER 5

CONCLUSION

The development efforts of an 8-bit digital throttling valve for a hybrid rocket motor are presented. The control valve technology utilizes a series of eight individually operated control valves set in parallel. Since the system divides the achievable total mass flow across all the valves, the required mass flow of any single valve remains low enough for solenoid operated valves (SOVs) to be used with flow restriction orifices attached downstream to alter the flow coefficient. This allows for rapid response times and precise control of the achievable total mass flow and thrust levels, which is only limited by the number of components in the digital valve design. An 8-bit prototype configuration was tested using a previously well characterized 98mm hybrid rocket motor that burns gaseous oxygen (GOX) and ABS plastic as propellants. Calibration tests performed on the 8-bit digital valve system show that the corrected orifice sizes on each SOV caused a reasonably linear mass flow and commanded throttle response.

Steady-state fuel regression rate calibration tests are used to empirically derive curve-fit coefficients for accurate fuel regression rate calculations. A testing campaign demonstrates multiple throttle profiles, including deep throttle ramp, deep throttle multi-step boxcar, and a 0.5 Hz frequency sine wave. The tests demonstrate that the motor can maintain combustion at a thrust level 10% of nominal thrust levels. Additional hot fire tests demonstrate that the 8-bit digital throttling valve can achieve a turndown ratio of about 40:1 and oxidizer mass flow rates of about 55 g/s with an injector pressure of around 400 psia. An investigation into the negative O/F ratio shift observed during the testing campaign revealed that the intensity of O/F ratio shift diminishes as the fuel port diameter grows over burn time. Comparison between the hot fire testing results and the 1-D hybrid combustion analytical model are also presented, showing good agreement.

As part of an analysis effort to investigate the latency and roll off issues in the performance data, a frequency response analysis was performed on both the deep throttle ramp and multi-step boxcar hot fire tests. The frequency response analysis results show that the digital valve is likely the biggest contributor to these latency and data rounding effects and that the fundamental frequency response of the end-to-end system is less than 10 Hz. The results of this thesis show that the 8-bit digital valve is an effective throttling technology and alternative to traditional position control valves. The digital throttling valve has the potential to significantly enhance the performance capabilities of hybrid rocket motors.

Lastly, follow on efforts to investigate the 8-bit digital throttling valve's ability to be used in the development of a feed-forward control scheme is discussed. The goal of this work is to overcome observed system latencies, and other distortions between actual and commanded throttle, including O/F ratio shift with closed-loop throttle compensation. Application of the discussed approach would generate a motor response that diminishes over time, resulting in a uniform thrust profile. Ongoing efforts in the USU PRL of using this throttling technology with the goal of developing an automatic O/F ratio shift compensating hybrid rocket motor is also discussed. Clearly the topic of digital throttling valve capabilities is expansive and rich for future research.

REFERENCES

[1] Anon, "Hazard Analysis of Commercial Space Transportation; Vol. 1: Operations, Vol. 2: Hazards, vol. 3: Risk Analysis," Tech. rep., Federal Aviation Administration, May 1988, https://www.faa.gov/about/office_org/headquarters_offices/ast/licenses_permits/media/hazard.pdf (accessed: September 29, 2023).

[2] Whitmore, S. A., Inkley, N. R., Merkley, D. P., and Judson, M. I., "Development of a Power-Efficient, Restart-Capable Arc Ignitor for Hybrid Rockets," *J. Prop. and Power*, Vol. 31, No. 6, 2015, pp. 1739–1749, https://arc.aiaa.org/doi/10.2514/1.B35595 (accessed: September 29, 2023).

[3] Whitmore, S. A., Mathias, S. D., and Harvey, R., "High Voltage Breakdown and Arc-Tracking Mechanism of Thermoplastics with Applications to Hybrid Rocket Arc-Ignition," *53rd AIAA/SAE/ASEE Joint Propulsion Conference*, AIAA 2017-4601, Atlanta, GA, July 2017, https://doi.org/10.2514/6.2017-4601 (accessed: September 29, 2023).

[4] Whitmore, S. A., Merkley, S. L., Tonc, L., and Mathias, S. D., "Survey of Selected Additively Manufactured Propellants for Arc Ignition of Hybrid Rockets," *J. Prop. and Power*, Vol. 32, No. 6, 2016, pp. 1494–1504, http://dx.doi.org/10.2514/1.B36106 (accessed: September 29, 2023).

[5] Whitmore, S. A. and Bulcher, A. M., "A Green Hybrid Thruster Using Moderately Enriched Compressed Air as the Oxidizer," *2018 Joint Propulsion Conference, AIAA Propulsion and Energy Forum*, AIAA 2018-4841, Cincinnati, OH, July 2018, https://doi.org/10.2514/6.2018-4841 (accessed: September 29, 2023).

[6] Whitmore, S. A., Peterson, Z. W., and Eilers, S. D., "Closed-Loop Precision Throttling of a Hybrid Rocket Motor," *J. Prop. and Power*, Vol. 30, No. 2, Feb. 2014, pp. 325–336, https://doi.org/10.2514/1.B34924 (accessed: October, 2, 2023).

[7] Whitmore, S. A., Spurrier, Z. S., Walker, S. D., and Merkley, S. L., "Throttled Launch-Assist Hybrid Rocket Motor for an Airborne NanoSat Launch Platform," *52nd AIAA/SAE/ASEE Joint Propulsion Conference*, AIAA 2016-4658, Salt Lake City, UT, July 2016, https://doi.org/10.2514/6.2016-4658 (accessed: October 2, 2023).

[8] Casalino, L. and Pastrone, D., "Integrated design-trajectory optimization for hybrid rocket motors," *Modeling and Optimization in Space Engineering*, Springer, New York, 2013, p. 343–363, https://link.springer.com/chapter/10.1007/978-1-4614-4469-5_14 (accessed: October, 2, 2023).

[9] Casalino, L. and Pastrone, D., ""A Straightforward Approach for Robust Design of Hybrid Rocket Engine Upper Stage," *51st AIAA/SAE/ASEE Joint Propulsion Conference*, AIAA 2015-4202, Orlando, FL, July 2015, https://doi.org/10.2514/6.2015-4202 (accessed: October 2, 2023).

[10] Casalino, L. and Pastrone, D., "Optimal Robust Design of Hybrid Rocket Engines," *Optimization and Its Applications*, Springer, New York, 2016, pp. 269–285, https://link.springer.com/chapter/10.1007/978-3-319-41508-6_10 (accessed: October, 2, 2023).

[11] Casalino, L., Masseni, F., and Pastrone, D., "Uncertainty Analysis and Robust Design for a Hybrid Rocket Upper Stage," *J. Spacecraft and Rockets*, Vol. 56, No. 6, March 2019, pp. 1–8, https://doi.org/10.2514/1.A34422 (accessed: October, 2, 2023).

[12] Betts, J. T., "Survey of Numerical Methods for Trajectory Optimization," *J. Guidance, Control, and Dynamics*, Vol. 21, No. 2, Feb. 1998, pp. 193–207, https://arc.aiaa.org/doi/10.2514/2.4231 (accessed: October, 2, 2023).

[13] Dornheim, M. A., "Reaching 100 km," *Av. Week Space Technol.*, Vol. 161, No. 6, 2004, pp. 45–46, https://www.researchgate.net/publication/292268464_Reaching_100_km (accessed: October, 2, 2023).

[14] Casalino, L. and Pastrone, D., "Optimization of Hybrid Sounding Rockets for Hypersonic Testing," *J. Prop. and Power*, Vol. 28, No. 2, 2012, pp. 405–411, https://doi.org/10.2514/1.B34218 (accessed: October, 2, 2023).

[15] Jens, E., Karp, A. C., Nakazono, B., Eldred, D. B., DeVost, M. E., and Vaughan, D., "Design of a Hybrid CubeSat Orbit Insertion Motor," *52nd AIAA/SAE/ASEE Joint Propulsion Conference*, AIAA 2016-4658, Salt Lake City, UT, July 2016, https://doi.org/10.2514/6.2016-4961 (accessed: October 2, 2023).

[16] Karp, A. C., Nakazono, B., Manrique, J. B., Shotwell, R., Vaughan, D., and Story, G. T., "A Hybrid Mars Ascent Vehicle Concept for Low Temperature Storage and Operation," *52nd AIAA/SAE/ASEE Joint Propulsion Conference*, AIAA 2016-4658, Salt Lake City, UT, July 2016, https://doi.org/10.2514/6.2016-4962 (accessed: October 2, 2023).

[17] Karabeyoğlu, A., Toson, E., and Evans, B., ""O/F Shift" in Hybrid Rockets," *50th AIAA/SAE/ASEE Joint Propulsion Conference*, AIAA 2014-3851, AIAA Propulsion and Energy Forum, Cleveland, OH, July 2014, https://doi.org/10.2514/6.2014-3851 (accessed: October 2, 2023).

[18] Waidmann, W., "Thrust Modulation in Hybrid Rocket Engines," *J. Prop. and Power*, Vol. 4, No. 5, 1988, pp. 421–427, https://doi.org/10.2514/3.23083 (accessed: October 4, 2023).

[19] Betts, E. M. and Federick, R. A., "Historical Systems Study of Liquid Rocket Engine Throttling Capabilities," *46th AIAA/SAE/ASEE Joint Propulsion Conference*, AIAA 2010-6541, Nashville, TN, July 2010, https://doi.org/10.2514/6.2010-6541 (accessed: October 4, 2023).

[20] Altman, D., "Hybrid Rocket Development History," *27th AIAA/SAE/ASEE Joint Propulsion Conference*, AIAA 1991-2515, Sacramento, CA, June 1991, https://doi.org/10.2514/6.1991-2515 (accessed: October 4, 2023).

[21] Moore, G. E. and Berman, K., "A Solid-Liquid Rocket Propellant System," *J. Jet Propulsion*, Vol. 26, No. 11, Nov. 1956, pp. 965–968, https://doi.org/10.2514/8.7170 (accessed: October 4, 2023).

[22] Duban, P., "The "LEX" rocket probe (LEX small rocket probe for in-flight testing of ONERA studies of hybrid propulsion, discussing design and program)," *L'Aeronautique et L'Astronautique*, Vol. 2, 1968, pp. 47–54.

[23] Franklin, B., Mead, J., and Bornhorst, B. R., "Certification Tests of a Hybrid Propulsion System for the Sandpiper Target Missile," Tech. rep., AFRPL-TR-69-73, 1969, https://apps.dtic.mil/sti/pdfs/AD0503586.pdf (accessed: October 4, 2023).

[24] Jones, R. A., ""Hybrid Propulsion System for an Advanced Rocket-Powered Target Missile," Tech. rep., Quarterly Technical Report, UTC 2220-QTR2, 1967.

[25] Penn, C. D. and Branigan, J. E., "Preliminary Flight Rating Tests of the HAST Propulsion System," Tech. rep., AFRPL-TR-15-5, 1975, https://apps.dtic.mil/sti/pdfs/ADA012200.pdf (accessed: October 4, 2023).

[26] Boardman, T. A., Carpenter, R. L., Goldberg, B. E., and Shaeffer, C. W., "Development and Testing of 11- and 24-inch Hybrid Motors under the Joint Government/Industry IR&D Program," *29th AIAA/SAE/ASEE Joint Propulsion Conference*, AIAA 1993-2552, Monterey, CA, June 1993, https://doi.org/10.2514/6.1993-2552 (accessed: October 4, 2023).

[27] Carpenter, R. L., Boardman, T. A., Claflin, S. E., and Harwell, R. J., "Hybrid Propulsion for Launch Vehicle Boosters: A Program Status Update," *31st AIAA/SAE/ASEE Joint Propulsion Conference*, AIAA 1995-2688, San Diego, CA, July 1995, https://doi.org/10.2514/6.1995-2688 (accessed: October 4, 2023).

[28] Wright, A. B., Warfield, T., Wright, A. M., and Wilson, E. W., "Instrumentation of UALR labscale hybrid rocket motor," *Proc. SPIE 6222*, Sensors for Propulsion Measurement Applications, May 2006, https://doi.org/10.1117/12.664620 (accessed: October 4, 2023).

[29] Austin, B. L., Heister, S. D., Dambach, E. M., and Meyer, S. E., "Variable Thrust, Multiple Start Hybrid Motor Solutions for Missile and Space Applications," *46tj AIAA/SAE/ASEE Joint Propulsion Conference*, AIAA 2010-7121, Nashville, TN, July 2010, https://doi.org/10.2514/6.2010-7121 (accessed: October 4, 2023).

[30] Whitmore, S. A., Peterson, Z. W., and Eilers, S. A., "Deep Throttle of a Nitrous Oxide and Hydroxyl Terminated Polybutadiene Hybrid Rocket Motor," *J. Prop. and Power*, Vol. 30, No. 1, 2014, pp. 78–86, https://doi.org/10.2514/1.B34967 (accessed: October 4, 2023).

[31] Whitmore, S. A., Walker, S. D., Merkley, S. L., and Spurrier, Z. S., "Throttled Launch-Assist Hybrid Rocket Motor for an Airborne NanoSat Launch Platform," *51st AIAA/SAE/ASEE Joint Propulsion Conference*, AIAA 2015-3940, Orlando, FL, July 2015, https://doi.org/10.2514/6.2015-3940 (accessed: October 4, 2023).

[32] Whitmore, S. A., Francom, M. W., Coombs, T. W., and Smith, A. N., "Development and Testing of a Fast-Acting, Deep-Throttling Hybrid Motor," (not yet published).

[33] Eilers, S. D. and Whitmore, S. A., "Correlation of Hybrid Rocket Propellant Regression Measurements with Enthalpy-Balance Model Predictions," *J. Spacecraft and Rockets*, Vol. 45, No. 5, Sept. 2008, https://doi.org/10.2514/1.33804 (accessed: October 9, 2023).

[34] Whitmore, S. A., "MAE 6530 Advanced Propulsion Systems, Section 3.3.1 Injector Notes," http://mae-nas.eng.usu.edu/MAE_6530_Web/New_Course/Section3/section.3.3.1.pdf (accessed: October 9, 2023).

[35] Anderson, J. D., *Modern Compressible Flow*, chap. 4, The McGraw Hill Companies, Inc, New York, 2003, pp. 127–187, https://libcat.lib.usu.edu/search/i0070016542 (accessed: October 9, 2023).

[36] Gordon, S. and McBride, B. J., "Computer Program for Calculation of Complex Chemical Equilibrium Compositions and Applications,," Tech. rep., NASA RP-1311, 1994, https://www1.grc.nasa.gov/research-and-engineering/ceaweb/ (accessed: October 9, 2023).

[37] Whitmore, S. A., "Variational Method for Estimating Time-Resolved Hybrid Fuel Regression Rates from Chamber Pressure," *AIAA Propulsion and Energy 2020 Forum*, AIAA 2020-3762, Virtual Event, Aug. 2020, https://doi.org/10.2514/6.2020-3762 (accessed: October 9, 2023).

[38] Whitmore, S. A., Frischkorn, C. I., and Petersen, S. J., "In-Situ Optical Measurements of Solid and Hybrid-Propellant Combustion Plumes," *Aerospace*, Vol. 9, No. 2, Jan. 2022, https://doi.org/10.3390/aerospace9020057 (accessed: October 9, 2023).

[39] Marxman, G. and Gilbert, M., "Turbulent Boundary Layer Combustion in the Hybrid Rockets," *Symposium (International) on Combustion*, Vol. 9, No. 1, 1963, pp. 371–383, https://doi.org/10.1016/S0082-0784(63)80046-6 (accessed: October 9, 2023).

[40] Marxman, G. A. and Muzzy, C. E. W. R. J., ""Fundamentals of Hybrid Boundary Combustion," *Progress Astronautics and Aeronautics*, Vol. 15, No. 1, 1964, pp. 485–492, https://doi.org/10.1016/B978-1-4832-2730-6.50025-7 (accessed: October 9, 2023).

[41] Emerson, *Frequency Analysis*, National Instruments, February 2023, https://www.ni.com/docs/en-US/bundle/labwindows-cvi/page/advancedanalysisconcepts/frequencyanalysis.html (accessed: January 23, 2024).

[42] Whitmore, S. A., "MAE 3340 Instrumentation Systems, Section 2.1: Introduction to Harmonic Analysis, Fourier Series, and the Continous Fourier Transform," http://mae-nas.eng.usu.edu/MAE_3340_Web/2015_Web_Page/section2/section2.2.pdf (accessed: January 23, 2024).

[43] Whitmore, S. A., "MAE 3340 Instrumentation Systems, Section 2.4: Notes on the Discrete Fourier Transform," http://mae-nas.eng.usu.edu/MAE_3340_Web/2015_Web_Page/section2/section2.4.pdf (accessed: January 23, 2024).

[44] Whitmore, S. A. and Merkley, S. L., "Radiation Heating Effects on Oxidizer-to-Fuel Ratio of Additively Manufactured Hybrid Rocket Fuels," *J. Prop. and Power*, Vol. 35, No. 4, 2019, pp. 863–878, https://doi.org/10.2514/1.B37037 (accessed: October 5, 2023).

[45] Whitmore, S. A., Bulcher, A. M., Lewis, Z., and Inkley, N., "Methods and Systems for Restartable Hybrid Rockets," Sept. 2020, https://patents.google.com/patent/US20150322892A1/en (accessed: October 14, 2023).